

POSSIBLE COUNTER ROTATION BETWEEN THE DISK AND PROTOSTELLAR ENVELOPE AROUND THE CLASS I PROTOSTAR IRAS 04169+2702

SHIGEHISA TAKAKUWA^{1,2}, YUSUKE TSUKAMOTO¹, KAZUYA SAIGO³, & MASAO SAITO⁴

¹Department of Physics and Astronomy, Graduate School of Science and Engineering, Kagoshima University, 1-21-35 Korimoto, Kagoshima, Kagoshima 890-0065, Japan; takakuwa@sci.kagoshima-u.ac.jp

²Academia Sinica Institute of Astronomy and Astrophysics, P.O. Box 23-141, Taipei 10617, Taiwan

³ALMA Project Office, National Astronomical Observatory of Japan, Osawa 2-21-1, Mitaka, Tokyo 181-8588, Japan

⁴TMT-J Project Office, National Astronomical Observatory of Japan, Osawa 2-21-1, Mitaka, Tokyo 181-8588, Japan

ABSTRACT

We present results from our SMA observations and data analyses of the SMA archival data of the Class I protostar IRAS 04169+2702. The high-resolution ($\sim 0''.5$) ^{13}CO (3–2) image cube shows a compact ($r \lesssim 100$ au) structure with a northwest (blue) to southeast (red) velocity gradient, centered on the 0.9-mm dust-continuum emission. The direction of the velocity gradient is orthogonal to the axis of the molecular outflow as seen in the SMA ^{12}CO (2–1) data. A similar gas component is seen in the SO (6_5-5_4) line. On the other hand, the C^{18}O (2–1) emission traces a more extended ($r \sim 400$ au) component with the opposite, northwest (red) to southeast (blue) velocity gradient. Such opposite velocity gradients in the different molecular lines are also confirmed from direct fitting to the visibility data. We have constructed models of a forward-rotating and counter-rotating Keplerian disk and a protostellar envelope, including the SMA imaging simulations. The counter-rotating model could better reproduce the observed velocity channel maps, although we could not obtain statistically significant fitting results. The derived model parameters are; Keplerian radius of 200 au, central stellar mass of $0.1 M_{\odot}$, and envelope rotational and infalling velocities of 0.20 km s^{-1} and 0.16 km s^{-1} , respectively. One possible interpretation for these results is the effect of the magnetic field in the process of disk formation around protostars, *i.e.*, Hall effect.

Keywords: ISM: molecules — ISM: individual (IRAS 04169+2702) — stars: formation

1. INTRODUCTION

Recent observational efforts have been finding Keplerian disks around not only T-Tauri stars (*e.g.*, Simon et al. 2000; Williams & Cieza 2011) but also protostars (Tobin et al. 2012; Harsono et al. 2014; Lindberg et al. 2014; Aso et al. 2015). The disks around protostars are considered to be under the formation and growth process of protoplanetary disks, precursors of planetary systems. Studies of disk formation processes around protostars are thus important to understand the initial condition of planet formation.

Theoretical studies have suggested that magnetic fields play a vital role in disk formation from protostellar envelopes (Li et al. 2014; Machida et al. 2016). The magnetic field connects the inner regions and the outer envelopes and efficiently transfers the angular momentum from the inner to outer regions. This process is known as magnetic braking (Gillis et al. 1974; Mouschovias 1985; Allen et al. 2003). If an ionization degree of the cloud cores is high enough and ideal magnetohydrodynamics (MHD) approximation is valid, the magnetic braking is so efficient and almost completely suppresses the circumstellar disk formation in cloud cores under a typical magnetic-field strength (Mellon & Li 2008; Hennebelle & Ciardi 2009). The ionization degree of the real cloud cores is, however, very low (Umebayashi & Nakano 1990; Nishi et al. 1991; Caselli et al. 1998; Nakano et al. 2002), and non-ideal MHD effects (Ohmic diffusion, Hall effect, and ambipolar diffusion) caused by low conductivity of the gas must play a role during the cloud core collapse. It has been suggested that the Ohmic and ambipolar diffusion decouples the magnetic field and the gas at $\rho > 10^{-12} \text{ g cm}^{-3}$ and circumstellar disk formation is enabled even at the very early phase of star formation (Machida et al. 2011a; Tsukamoto et al. 2015a; Tomida et al. 2015; Masson et al. 2016). Recent theoretical simulations show that the Hall effect imprints the characteristic velocity structure in the envelope and disk, *i.e.*, a flip of the rotation velocity, or counter rotation (Krasnopolsky et al. 2011; Li et al. 2011; Tsukamoto et al. 2015b;

Wurster et al. 2016; Tsukamoto et al. 2017).

Another important physical mechanism that controls disk formation is turbulence. Theoretical simulations show that turbulence can reduce the magnetic braking through magnetic diffusions and reconnections, and add additional angular momenta (Santos-Lima et al. 2012; Joos et al. 2013; Seifried et al. 2013; Matsumoto et al. 2017). Such turbulent effects promote disk formation around protostars. Furthermore, the rotational axis of the formed disk can be misaligned from that of the surrounding protostellar envelope (Matsumoto et al. 2017).

It has been difficult, however, to observationally identify gas motions which are indeed controlled by magnetic fields or turbulence in disk-forming regions. Detailed observational comparisons of gas motions from dense cores, envelopes, to central disks are essential to tackle this problem (Tobin et al. 2011; Harsono et al. 2014). In particular, radial rotational profiles from the envelope to the inner disk have been measured observationally (Yen et al. 2013; Harsono et al. 2014; Harsono et al. 2015; Aso et al. 2015). Those observations show that the radial rotational profiles in the envelopes and disks can be approximated to be $v_{rot} \sim r^{-1}$ and $\sim r^{-0.5}$, that is, rotation with the conserved specific angular momenta and Keplerian rotation, respectively. While these results apparently show that the magnetic or turbulent effect on the gas motions is not significant, the rotational profiles and the power-law indices derived from these observations are not accurate enough to be directly compared with those from theoretical simulations.

A more straightforward observational signature of such effects is desirable. We consider that change of the rotational axes between the central disk and the outer envelope, or even the flip of the rotational vectors, is an intriguing tracer for the effect of magnetic field and turbulence. In this paper, we report SubMillimeter Array (SMA)¹ observations of IRAS 04169+2702 at 330 GHz as well as data analyses of the SMA archival data at 230 GHz. IRAS 04169+2702 (hereafter I04169) is a Class I protostar ($L_{bol} = 0.76 L_{\odot}$; $T_{bol} = 133$ K) (Kenyon et al. 1993a; Kenyon et al. 1993b; Young et al. 2003) located in the molecular filament of the B213 / L1495 region at $d = 140$ pc (Hacar et al. 2013; Tafalla & Hacar 2015). The protostar is associated with a ~ 20000 AU scale, $\sim 1 M_{\odot}$ dense core as seen in the 1.3-mm and 850 μm dust-continuum (Motte & André 2001; Young et al. 2003) and N_2H^+ (1–0) emission (Tatematsu et al. 2004). Previous millimeter interferometric observations of I04169 in the C^{18}O (1–0) (Ohashi et al. 1997) and H^{13}CO^+ (1–0) lines (Saito et al. 2001) have found a $r \sim 1000$ au scale protostellar envelope elongated along the northwest to southeast direction (P.A. = 154°) with an inclination angle of $i \sim 60^\circ$. In the C^{18}O (1–0) line, the southeastern part of the envelope is blueshifted (~ -0.8 km s $^{-1}$ from $v_{sys} = 6.8$ km s $^{-1}$) and northwestern part redshifted ($\sim +0.8$ km s $^{-1}$), and this velocity gradient along the major axis is regarded as the rotation of the envelope (Ohashi et al. 1997). CARMA 1.3-mm continuum and Keck I-band imaging of I04169 exhibit a small, almost unresolved ($\lesssim 1''$) dusty disk without any scattered light (Eisner 2012).

From the SMA data of I04169, we have found possible observational evidence for a counter rotation between the protostellar envelope and circumstellar disk, which will be shown in the rest of the present paper. In Section 2, we shall describe our new SMA observations and archival data, and calibrations and imaging of those data. In Section 3, the 0.9-mm and 1.3-mm continuum, ^{12}CO (2–1), ^{13}CO (2–1; 3–2), C^{18}O (2–1), and SO (6 $_5$ –5 $_4$) results are presented and compared. Section 4 describes our modeling efforts to reproduce the observed velocity structures with the SMA. In Section 5.1 we discuss physical origin of the observed gas motions around I04169 and in section 5.2 implications of these results.

2. SMA OBSERVATIONS AND DATA REDUCTION

SMA Observations of I04169 at 330 GHz were made on 2014 December 19 and 2015 February 6 with its very extended and extended configurations, respectively. Details of the SMA are described by Ho et al. (2004). The correlator covered the ^{13}CO ($J=3-2$; 330.588 GHz), C^{18}O ($J=3-2$; 329.331 GHz) and the CS ($J=7-6$; 342.883 GHz) lines, and the spectral windows (“chunks”) of the correlator with 512 channels were assigned to these lines. The bandwidth of one chunk is 82 MHz, and thus the spectral resolution of these lines is 203.125 kHz. In each sideband there were a total of 48 chunks, and all the chunks at both sidebands except for those assigned to the lines were combined to make a single continuum channel. The central frequency of the continuum channel is ~ 336.933 GHz ($\lambda \sim 0.89$ mm), and hereafter the continuum emission is called as the 0.9-mm continuum emission. The minimum projected baseline length was $\sim 29 k\lambda$ at the ^{13}CO (3–2) frequency, and for a Gaussian emission distribution with an FWHM of $\sim 5''.7$ (~ 800 AU), the peak flux density recovered is $\sim 10\%$ of the peak flux density of the Gaussian (Wilner & Welch 1994). The uncertainty in the absolute flux calibration is inferred to be $\sim 30\%$. Table 1 summarizes the observational parameters.

¹ The SMA is a joint project between the Smithsonian Astrophysical Observatory and the Academia Sinica Institute of Astronomy and Astrophysics and is funded by the Smithsonian Institution and the Academia Sinica.

SMA archival data of I04169 at 230 GHz taken in 2011 December 15 and 2012 February 15 with the compact and extended configurations, respectively, were retrieved and re-calibrated. The data include the ^{12}CO ($J=2-1$), ^{13}CO ($J=2-1$), C^{18}O ($J=2-1$), and the SO ($J_N=6_5-5_4$) lines. The SMA chunks with 512 channels were allocated to the three CO isotopic lines, while a chunk with 128 channels to the SO line. The central frequency of the continuum channel is ~ 225.506 GHz ($\lambda \sim 1.33$ mm), and hereafter the continuum emission is called as the 1.3-mm continuum emission. Unfortunately, the spectral setting was not optimized to the C^{18}O ($2-1$) line, and the C^{18}O spectral region with $V_{\text{LSR}} > 7.6$ km s $^{-1}$ was dropped out of the chunk with 512 channels. In contrast to the 330 GHz observations described above, the 230 GHz observations cover a factor ~ 3 shorter spacings, and the minimum projected baseline length (~ 9.9 k λ) at the C^{18}O ($2-1$) frequency implies that for a Gaussian emission distribution with an FWHM of $\sim 16''.7$ (~ 2300 AU), the peak flux density recovered is $\sim 10\%$ of the peak flux density of the Gaussian (Wilner & Welch 1994). On the other hand, the angular resolution of the 230 GHz observations is limited to $\sim 1''.5$, while that of the 330 GHz observations is as high as $\lesssim 0''.5$. These facts imply that the 230 GHz observations are more suitable to investigate the protostellar envelope around I04169, while the 330 GHz observations to study the central disk. Table 2 summarizes the parameters of the 230 GHz observations.

The raw visibility data were calibrated with an IDL-based reduction package, MIR (Scoville et al. 1993), and the calibrated visibility data were Fourier-transformed and CLEANed with MIRIAD (Sault et al. 1995). Depending on the intensities of the observed molecular lines different visibility weightings were adopted to construct the images. The Natural weighting and $0''.3$ tapering were applied to the ^{13}CO ($3-2$) visibility data, to recover enough fluxes and to construct the image cube with a sufficient signal-to-noise ratio. With the same visibility weighting and tapering the C^{18}O ($3-2$) emission is only marginally detected above 4σ ($1\sigma = 0.13$ J beam $^{-1}$) at $V_{\text{LSR}} = 5.8$ and 6.0 km s $^{-1}$, and there is no CS ($7-6$) emission detected. The Natural weighting and $2''.0$ tapering are applied to the C^{18}O ($2-1$) visibility data to recover enough fluxes of the protostellar envelope. The adopted visibility weightings and the resultant beam sizes and the noise levels of the different molecular-line data are summarized in Table 3. Regarding the continuum data both the Natural and Uniform weightings were adopted to investigate the changes of the continuum images with the two extreme weightings (see the next section).

Table 1. Parameters for the SMA Observations of I04169 at 330 GHz

Parameter	Value	
	2014 December 19	2015 February 6
Number of Antennas	7	5
Configuration	Very Extended	Extended
Right ascension (J2000.0)	04 ^h 19 ^m 58 ^s .45	
Declination (J2000.0)	27° 09' 57''.1	
Primary Beam HPBW	$\sim 37''$	
Baseline Coverage	29 - 561 (k λ)	
Conversion Factor (^{13}CO)	1 (Jy beam $^{-1}$) = 38.7 (K)	
Continuum Bandwidth	7.87 GHz	
Flux Calibrator	3c84	Callisto
Gain Calibrator	3c84, 3c111	
Flux (3c84)	7.6 Jy	7.4 Jy
Flux (3c111)	0.93 Jy	0.91 Jy
Passband Calibrator	3c279	
System Temperature	$\sim 400 - 1200$ K	$\sim 300 - 700$ K

Table 2. Parameters for the SMA Archival Data of I04169 at 230 GHz

Parameter	Value	
	2011 December 15	2012 February 15
Number of Antennas	8	
Configuration	Compact	Extended
Right ascension (J2000.0)	04 ^h 19 ^m 58 ^s .44	
Declination (J2000.0)	27° 09' 57".0	
Primary Beam HPBW	~56"	
Baseline Coverage	10 - 164 (kλ)	
Conversion Factor (C ¹⁸ O)	1 (Jy beam ⁻¹) = 2.83 (K)	
Continuum Bandwidth	6.48 GHz	
Flux Calibrator	Callisto	Uranus
Gain Calibrator	3c84, 3c111	
Flux (3c84)	8.8 Jy	8.4 Jy
Flux (3c111)	2.3 Jy	2.4 Jy
Passband Calibrator	3c279	3c279, Mars
System Temperature	~200 - 500 K	~150 - 300 K

Table 3. Summary of the Line Images

Line	Frequency (GHz)	Weighting	Beam (P.A.)	Velocity Resolution (km s ⁻¹)	rms (Jy beam ⁻¹)
¹³ CO ($J=3-2$)	330.587965	Natural, 0''3 taper	0''59×0''49 (86°)	0.18	0.12
C ¹⁸ O ($J=2-1$)	219.560358	Natural, 2''0 taper	3''09×2''90 (-69°)	0.28	0.099
¹² CO ($J=2-1$)	230.538000	Uniform	1''54×1''37 (-80°)	0.26	0.14
¹³ CO ($J=2-1$)	220.398684	Natural	1''82×1''52 (-88°)	0.28	0.060
SO ($J_N=6_5-5_4$)	219.949433	Natural	1''82×1''52 (-88°)	1.11	0.028

3. RESULTS

3.1. Continuum and CO Outflow

Figure 1 shows the 0.9-mm and 1.3-mm dust-continuum images of I04169 at the Natural and Uniform weightings, and Table 4 summarizes their image quantities. The 1.3-mm continuum emission is not resolved with the present angular resolution of $\sim 1''.5$. Even with the higher-resolution observations at 0.9-mm the dust-continuum emission is barely resolved, and the beam-deconvolved emission sizes are as small as the beam sizes (Table 4). In the Natural-weighted 0.9-mm continuum image there appears a marginal emission extension to the east, but this component is degraded in the Uniform-weighted image. These results indicate that from the continuum images it is not possible to identify the direction of the major axis of the circumstellar disk. In the following, we regard the centroid position of the 0.9-mm continuum image with the Natural weighting measured from the 2-dimensional Gaussian fitting as the protostellar position (04^h 19^m 58^s.463, 27° 09' 56".936).

From the continuum flux densities derived from the Natural-weighted images at the two frequency bands, plus the continuum flux density at 2.7 mm (~ 17 mJy; Ohashi et al. 1997), the spectral index α is calculated to be $\alpha \sim 2.19 \pm 0.25$. The measured α value indicates a small β value, *i.e.*, $\beta \sim 0-0.5$, suggesting dust growths. The mass of the dusty component around I04169 ($\equiv M_d$) is estimated from the measured 0.9-mm continuum flux density ($\equiv S_\nu$) at the Natural weighting as;

$$M_d = \frac{S_\nu d^2}{\kappa_\nu B_\nu(T_d)}, \quad (1)$$

where ν is the frequency, d the distance, $B_\nu(T_d)$ the Planck function for dust at a temperature T_d , and κ_ν the dust opacity per unit gas + dust mass on the assumption of a gas-to-dust mass ratio of 100. The mass opacity at 0.9 mm is calculated to be $\kappa_{0.9mm} = 0.053 \text{ cm}^2 \text{ g}^{-1}$ from $\kappa_\nu = \kappa_{\nu_0} (\nu/\nu_0)^\beta$, $\kappa_{250 \mu m} = 0.1 \text{ cm}^2 \text{ g}^{-1}$ (Hildebrand 1983), and $\beta=0.5$. For $T_d = 10 - 30 \text{ K}$, the mass of the dusty circumstellar material is calculated to be $0.0042 - 0.024 M_\odot$. The adopted dust mass opacity is a factor 3 higher than that of Ossenkopf & Henning (1994) for grains with thin ice mantles coagulated at a density of 10^6 cm^{-3} ($\kappa_{0.9mm} = 0.018 \text{ cm}^2 \text{ g}^{-1}$). Thus, adopting the dust mass opacity by Ossenkopf & Henning (1994) yields a factor 3 higher mass.

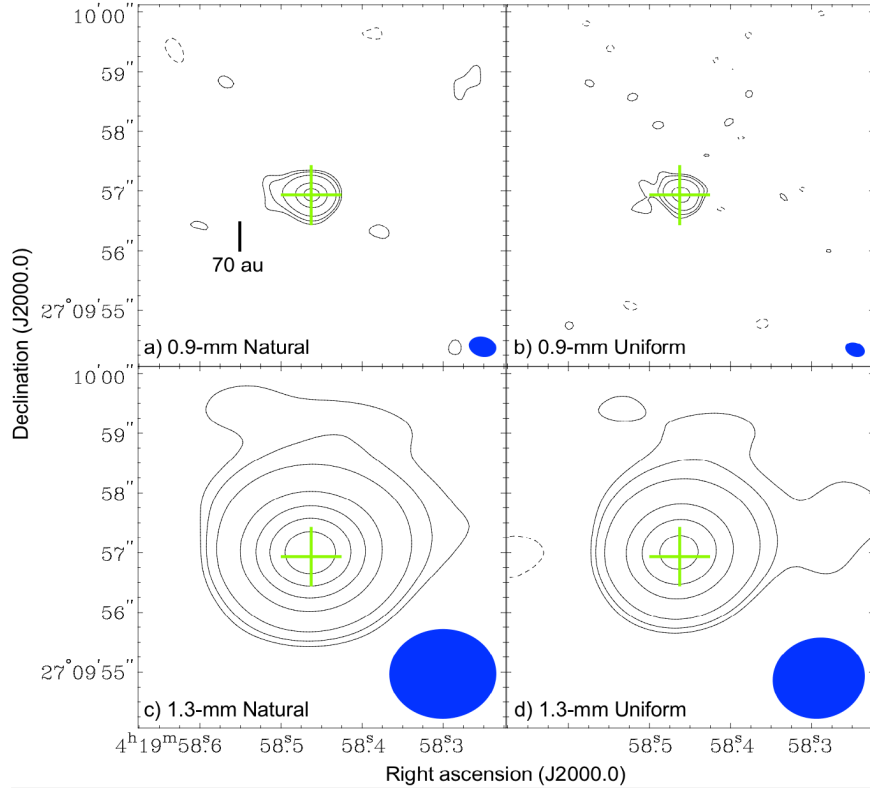


Figure 1. SMA continuum images of I04169. Contour levels are 3σ , 5σ , 10σ , 30σ , 50σ , 70σ , 90σ , 110σ , where 1σ levels are summarized in Table 4. Crosses show the centroid position of the 0.9-mm continuum image with the Natural weighting, which we regard as the position of the protostar. Filled ellipses at the bottom-right corners show the synthesized beams, which are also summarized in Table 4.

Table 4. 1.3-mm and 0.9-mm Continuum Results of I04169

λ	Weighting	Beam (P.A.)	rms (mJy)	Flux Density (Jy) ^a	Deconvolved Size ^a
1.3 mm	Natural	$1''.76 \times 1''.50$ (-89°)	0.84	0.088	...
	Uniform	$1''.52 \times 1''.35$ (-78°)	1.1	0.085	...
0.9 mm	Natural	$0''.46 \times 0''.34$ (76°)	2.2	0.189	$0''.30 \times 0''.23$ (-70°)
	Uniform	$0''.33 \times 0''.23$ (68°)	2.2	0.180	$0''.27 \times 0''.25$ (-46°)

^a Derived from the 2-dimensional Gaussian fitting to the continuum images shown in Figure 1.

Figure 2 shows distributions of the blueshifted and redshifted ^{12}CO (2–1) and ^{13}CO (2–1) emission in I04169. For comparison, the directions of the associated outflow measured from the ^{12}CO (1–0) observations (P.A.= 64° ; dashed line along the NE-SW direction) and the major axis of the $r \sim 1000$ -au scale protostellar envelope as seen in the C^{18}O (1–0) emission (P.A.= 154° ; dashed line along the NW-SE direction) are also shown (Ohashi et al. 1997). These two

axes are orthogonal with each other. The redshifted ^{12}CO (2–1) emission exhibits a tilted U -shaped feature with its symmetric axis consistent with the ^{12}CO (1–0) outflow axis. The blueshifted ^{12}CO (2–1) emission shows a tilted V -shaped feature with its apex close to the protostellar position. The symmetric axis of the blueshifted emission is also consistent with the ^{12}CO (1–0) outflow axis. These results indicate that the ^{12}CO (2–1) emission also traces the molecular outflow driven from I04191. There are other possible emission components, such as the 7σ redshifted peak to the northeast of the protostar and the 5σ blueshifted peak to the southwest, as they appear consecutively in the velocity channel maps. The redshifted ^{13}CO (2–1) emission to the east of the protostar appears to trace the outflow component too. On the other hand, the blueshifted ^{13}CO (2–1) emission is compact and located to the northwest of the protostar, and thus its origin is likely distinct from that of the blueshifted ^{12}CO (2–1) emission (*i.e.*, outflow). The origin of the elongated redshifted ^{13}CO (2–1) emission to the west of the protostar is not clear. As the elongation is along the outflow axis, this component may trace the part of the outflow components located to the other side from the plane of the sky.

There must also be an underlying extended cloud component of the ^{12}CO and ^{13}CO (2–1) emission. Interferometric observations of such extended emission structures are challenging and often produce sidelobe features, which are difficult to remove even with CLEAN. The apparently noisier images in Figure 2 likely reflect such an imperfectness of the deconvolution process.

From these outflow and previous results of the protostellar envelope as seen in the C^{18}O (1–0) emission, the position angle of the major axis of the protostellar envelope is regarded as P.A.= 154° .

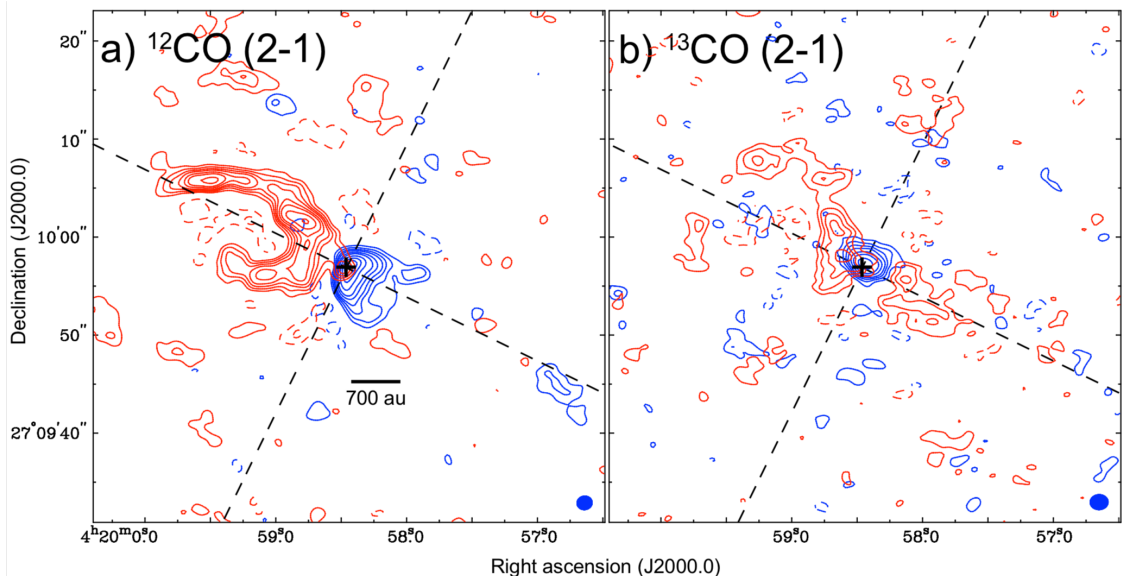


Figure 2. a) SMA images of the blueshifted ($V_{\text{LSR}} = 0.13 - 5.94 \text{ km s}^{-1}$) and redshifted ($7.79 - 15.19 \text{ km s}^{-1}$) ^{12}CO (2–1) emission in I04169. Contour levels are 3σ , 5σ , 7σ , 9σ , 12σ , 15σ , and then in steps of 5σ ($1\sigma = 0.17 \text{ Jy beam}^{-1} \text{ km s}^{-1}$ and $0.20 \text{ Jy beam}^{-1} \text{ km s}^{-1}$ for the blueshifted and redshifted emission.). A cross show the position of the protostar, and a filled ellipse at the bottom-right corner the synthesized beam ($1''.54 \times 1''.37$; P.A.= -80°). Dashed lines denote the position angles of 154° and 64° , which are regarded as the major and minor axes of the envelope around I04169, respectively. b) SMA images of the blueshifted ($3.21 - 6.80 \text{ km s}^{-1}$) and redshifted ($6.80 - 10.39 \text{ km s}^{-1}$) ^{13}CO (2–1) emission in I04169. Contour levels are 3σ , 5σ , 7σ , 9σ , 12σ , 15σ , and then in steps of 5σ ($1\sigma = 0.060 \text{ Jy beam}^{-1} \text{ km s}^{-1}$). A filled ellipse at the bottom-right corner shows the synthesized beam ($1''.82 \times 1''.52$; P.A.= -88°).

3.2. C^{18}O (2–1), SO (6_5-5_4), and ^{13}CO (3–2)

Figure 3 shows velocity channel maps of the C^{18}O (2–1) emission in I04169. At $V_{\text{LSR}} = 5.26 - 5.54 \text{ km s}^{-1}$, there is an unresolved, weak C^{18}O (2–1) component to the north of the protostar. In the lower blueshifted velocities ($5.82 - 6.66 \text{ km s}^{-1}$), the C^{18}O (2–1) emission is located to the southwest of the protostar. In the redshifted velocities ($6.94 - 7.22 \text{ km s}^{-1}$) the emission peak is shifted to the northwest and then north. Thus, in the low-velocity C^{18}O (2–1) emission the northern part is redshifted and the southern part blueshifted, which is consistent with the velocity gradient of the $r \sim 1000$ -au scale protostellar envelope (Ohashi et al. 1997). The outermost extent of these low-velocity C^{18}O (2–1) emission is $r \sim 400$ au. Because of the correlator setting of the SMA archival data, the C^{18}O (2–1) emission

in the higher redshifted velocities was not observed. We have checked the phase and amplitude behaviors in the C^{18}O (2–1) visibility spectra at the chunk edge. The behaviors appear normal. Specifically, the C^{18}O visibility spectrum taken with the compact configuration shows a systematic phase trend changing from $\sim +20^\circ$ to -20° from channel 500 to 511, with an approximate rms of $\sim 10^\circ$. This systematic phase trend reflects the observed north (red) to south (blue) velocity gradient. On the other hand, the C^{18}O visibility spectrum taken with the extended configuration, which is significantly down-weighted in the imaging process (see section 2), is undetected. We consider that there is no significant edge effect of the SMA chunk, which affects the observed C^{18}O (2–1) velocity gradient.

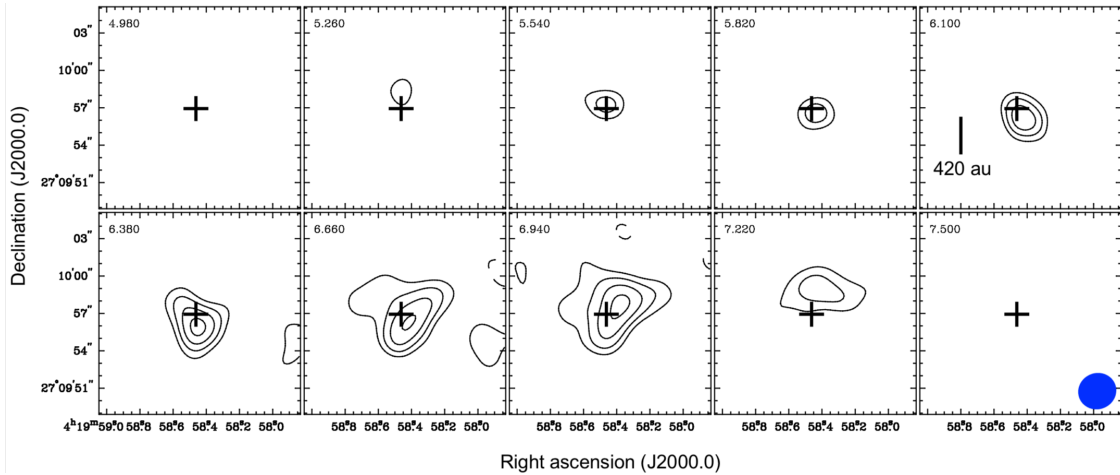


Figure 3. Velocity channel maps of the C^{18}O (2–1) emission in I04169. Contour levels are 3σ , 4σ , 5σ , 6σ ($1\sigma = 0.099 \text{ Jy beam}^{-1}$). Crosses show the protostellar position, and a filled ellipse at the bottom-right corner the synthesized beam ($3''.09 \times 2''.90$; P.A. = -69°).

Figure 4 presents velocity channel maps of the SO (6_5-5_4) emission in I04169. The SO emission is intense, and without any uv tapering sufficient SO flux densities are recovered within a finer beam size ($1''.82 \times 1''.52$) than that of the C^{18}O (2–1) image cube. The image area in Figure 4 is correspondingly smaller than that in Figure 3. The velocity resolution of the SO image cube is, on the other hand, a factor 4 worse than that of the C^{18}O (2–1) image cube. In the highly blueshifted ($V_{LSR} = 5.14 \text{ km s}^{-1}$) and redshifted (8.46 km s^{-1}) velocities, compact SO emission is seen to the north and south of the protostar, respectively. The outermost extent of the high-velocity SO emission is $r \sim 200 \text{ au}$. The peaks of the low-velocity blueshifted (6.25 km s^{-1}) and redshifted (7.35 km s^{-1}) SO emission are also located to the north and south. The sense of this SO velocity gradient is opposite to that of the C^{18}O (2–1) emission and the $r \sim 1000\text{-au}$ scale protostellar envelope. In the low-velocity range, there is also an emission feature elongated approximately perpendicular to the outflow axis.

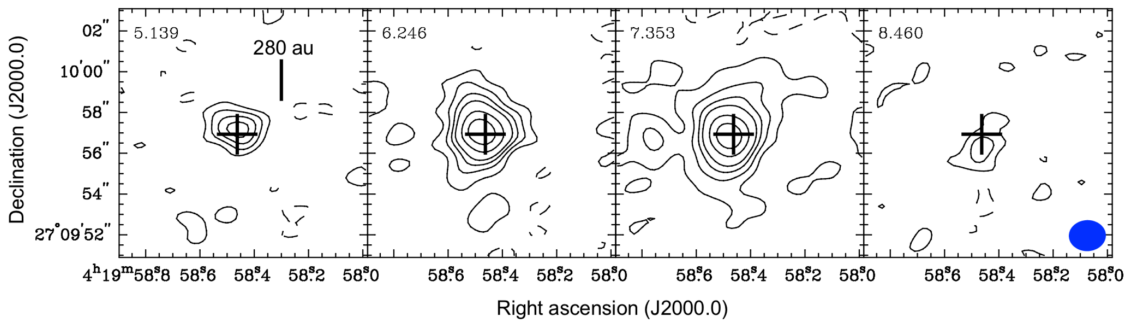


Figure 4. Velocity channel maps of the SO (6_5-5_4) emission in I04169. Contour levels are 2σ , 4σ , 6σ , 8σ , and then in steps of 4σ ($1\sigma = 0.027 \text{ Jy beam}^{-1}$). Crosses show the protostellar position, and a filled ellipse at the bottom-right corner the synthesized beam ($1''.82 \times 1''.52$; P.A. = -88°).

Figure 5 shows velocity channel maps of the ^{13}CO (3–2) emission in I04169. The higher angular-resolution ($\sim 0''.5$)

image cube reveals a velocity structure of molecular gas in the vicinity ($r \sim 100$ au) of the protostar. Note that the angular resolution of this image cube is a factor ~ 6 higher than that of the C^{18}O (2–1) image cube described above. For a clear presentation, the image region of Figure 5 is set to be a factor $\sim 4^2$ smaller than that of the C^{18}O (2–1) image. In the blueshifted velocity range ($V_{LSR}=3.8\text{--}5.6$ km s^{-1}), there are ^{13}CO (3–2) emission peaks located to the northwest of the protostar. This blueshifted velocity range approximately matches that of the SO velocity channel at $V_{LSR}=5.14$ km s^{-1} , where the SO emission is also located to the north (Figure 4). There is also a weak C^{18}O (2–1) component seen to the north at $V_{LSR} = 5.26 - 5.54$ km s^{-1} , consistent with the ^{13}CO (3–2) velocity range. Therefore, the northern highly blueshifted gas component is likely seen in all the three tracers. At $V_{LSR} = 5.6$ km s^{-1} , another ^{13}CO (3–2) emission component to the southwest of the protostar is seen. As the location of this emission component is close to the outflow axis and the southwestern side corresponds to the blueshifted outflow side (Figure 2), this emission component is likely to trace the outflow. In the lower velocity range at $v_{sys} (= 6.8$ km $\text{s}^{-1}) \pm 0.6$ km s^{-1} , the ^{13}CO (3–2) emission appears to be severely suppressed. This is presumably due to the presence of a foreground, intervening molecular cloud material, which absorbs the ^{13}CO (3–2) emission associated with the Class I object. In these velocities, the low-velocity C^{18}O (2–1) emission exhibits a south (blue) to north (red) velocity gradient as described above (Figure 3). In the redshifted velocity range ($V_{LSR} = 8.0\text{--}9.2$ km s^{-1}), the ^{13}CO (3–2) emission is located to the southeast and south of the protostar. This redshifted velocity range is approximately consistent with that of the SO velocity channel at $V_{LSR}=8.46$ km s^{-1} , where the SO emission is also located to the south (Figure 4).

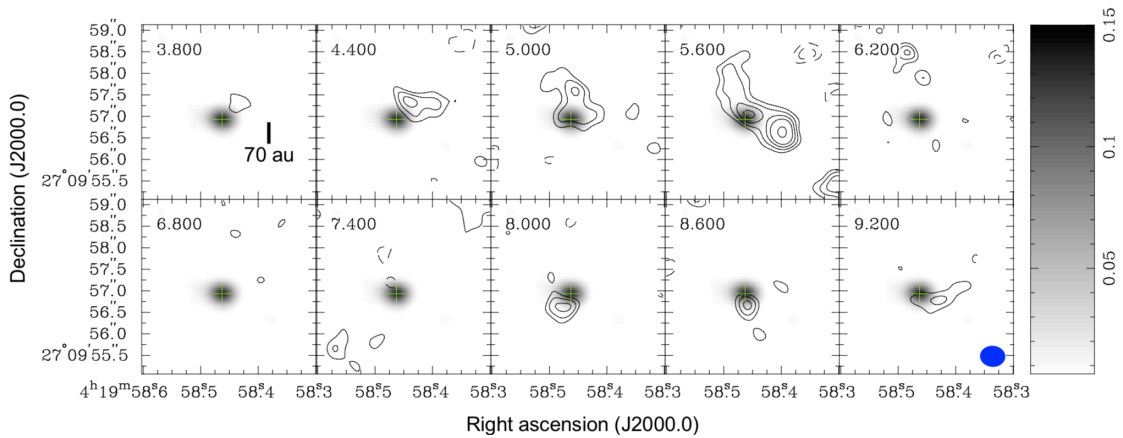


Figure 5. Velocity channel maps of the ^{13}CO (3–2) emission at every 0.6 km s^{-1} bin (contours), superposed on the 0.9 -mm dust-continuum image with the Natural weighting (gray), in I04169. Contour levels are 3σ , 4σ , 5σ , 6σ , and then in steps of 2σ ($1\sigma = 69$ mJy beam^{-1}). Crosses show the protostellar position. A filled ellipse at the bottom-right corner shows the synthesized beam ($0''.59 \times 0''.49$; P.A. = 86°).

Figure 6 compares the detected velocity features in the different molecular tracers at different spatial scales. In the ^{13}CO (3–2) emission, the high-velocity blueshifted and redshifted components are located to the northwest and southeast of the protostar, respectively (Figure 6a). The outermost extent of the ^{13}CO (3–2) emission is $r \sim 100$ au. The apparently noisier image of the ^{13}CO (3–2) map is presumably due to the contamination from an extended, foreground absorbing material. In the ^{13}CO (3–2) velocity channel maps (Figure 5), the beam size is $0''.589 \times 0''.490 \sim 0''.537$ (geometrical mean), and the peak S/N are 5.5σ , 5.2σ , 6.3σ , 5.3σ , and 5.3σ at $V_{LSR} = 4.4$ km s^{-1} , 5.0 km s^{-1} , 5.6 km s^{-1} , 8.0 km s^{-1} , and 8.6 km s^{-1} , respectively. Thus the positional accuracy at each velocity channel should be better than $\sim 0''.537 / 5.2\sigma \sim 0''.103$. The angular separation between the blueshifted and redshifted emission is $\sim 0''.65$ (Figure 6a), and thus this separation between the blueshifted and redshifted velocities (*i.e.*, velocity gradient) is detected at least above $\sim 0''.65 / 0''.103 \sim 6.3\sigma$. If the blueshifted and redshifted emission are integrated as shown in Figure 6a, the peak S/N of the blueshifted and redshifted emission are 8.5σ and 7.4σ , respectively. Thus the significance of the velocity gradient is raised to $\sim 0''.65 / 0''.537 / 7.4\sigma \sim 9.0\sigma$. These estimates show that the detected northwest (blue) to southeast (red) velocity gradient in the ^{13}CO (3–2) emission is statistically robust. Furthermore, the direction of the velocity gradient approximately matches with the major axis of the protostellar envelope, and the axis orthogonal to the outflow direction. The peak locations of the integrated blueshifted and redshifted SO ($6_5\text{--}5_4$) emission appear to match with those of the ^{13}CO (3–2) emission, although the spatial resolution of the SO map is factor ~ 3 worse (Figure 6b).

On the other hand, in the lower-velocity range where the ^{13}CO (3–2) emission is significantly suppressed, the blueshifted and redshifted C^{18}O (2–1) emission are located to the south and north of the protostar, respectively, with the outermost extent of $r \sim 400$ au (Figure 6c). The sign of the C^{18}O (2–1) velocity gradient is opposite to that of the inner ^{13}CO (3–2) and SO (6₅–5₄) emission. Furthermore, the direction of the axis connecting the peaks of the blueshifted and redshifted C^{18}O (2–1) emission is along north to south, rather than northwest to southeast. This indicates that there is also a slight velocity gradient in the C^{18}O (2–1) emission along the minor axis, and the northeastern part is slightly more redshifted and southwestern part more blueshifted. There is also a compact, high-velocity blueshifted C^{18}O (2–1) emission located to the north of the protostar (Figure 6d). As the spatial location and the velocity range of this C^{18}O (2–1) emission component is consistent with those of the blueshifted ^{13}CO (3–2) emission, the origin of the high-velocity blueshifted C^{18}O (2–1) emission is likely the same as that of the ^{13}CO (3–2) emission.

To further verify the presence of the opposite velocity gradients between the ^{13}CO , SO , and the C^{18}O emission, we have also fit 2-dimensional Gaussians to the observed visibility data and derived the emission peak positions at different velocity bins. The velocity bins are chosen to match with those of the relevant velocity channel maps (Figures 3, 4, 5), except for the high-velocity blueshifted C^{18}O emission (Figure 6d). A single 2-dimensional Gaussian is fitted to the visibility at each velocity bin, except for the ^{13}CO (3–2) emission at $V_{LSR} = 5.6$ km s⁻¹ where three Gaussians are adopted. The fitting results are summarized in Figure 7. In the ^{13}CO (3–2) visibility fitting, the blueshifted positions are clustered to the north and northwest while the redshifted positions to the south. This trend reflects the well-separated blueshifted and redshifted emission as shown in Figure 6a. The two blue- and redshifted points of the SO emission are also well separated and located to the north and south, respectively. On the other hand, in the case of the C^{18}O emission two redshifted points are located to the north while the four blueshifted points to the south. The exception is the high-velocity blueshifted C^{18}O emission located to the north. These visibility analyses demonstrate that the velocity structures and the flip of the velocity gradient between the ^{13}CO , SO , and the C^{18}O emission identified in the images (Figure 6) are also present in the visibility domain, and are unlikely due to the interferometric imaging effect.

Table 5 summarizes the detected velocity gradients along the major axis.

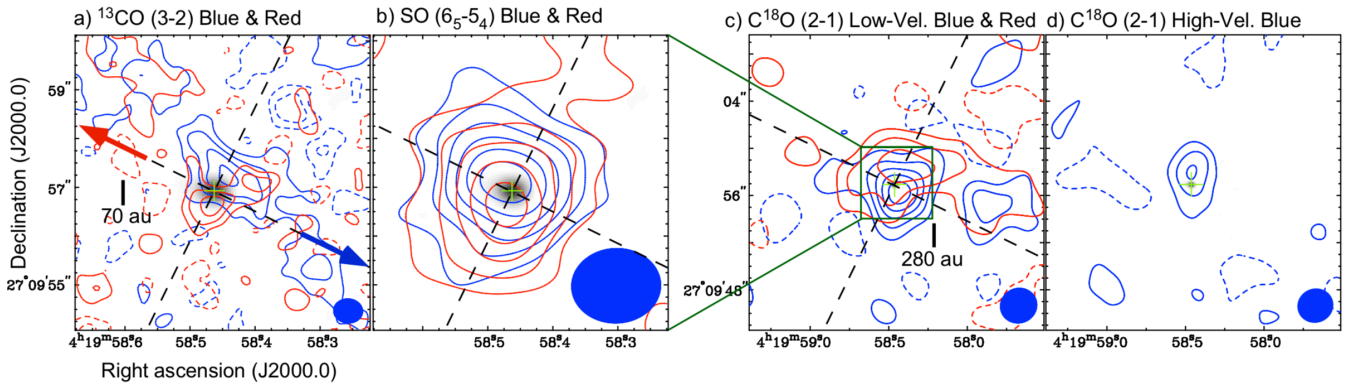


Figure 6. a) Maps of the blueshifted (blue contours) and redshifted (red) ^{13}CO (3–2) emission, superposed on the 0.9-mm dust-continuum image (gray), in I04169. The integrated velocity ranges for the blueshifted and redshifted emission are $V_{LSR} = 3.7 - 5.9$ km s⁻¹ and $7.5 - 9.3$ km s⁻¹, respectively. Contour levels are in steps of 2σ , where 1σ noise levels are 80 mJy beam⁻¹ km s⁻¹ and 72 mJy beam⁻¹ km s⁻¹ for the blueshifted and redshifted emission, respectively. A cross shows the position of the protostar. Dashed lines denote the major and minor axes of the protostellar envelope. Blue and red arrows show the directions of the blueshifted and redshifted outflows (Figure 2). A filled ellipse at the bottom-right corner shows the synthesized beam ($0''.59 \times 0''.49$; P.A. = 86°). b) Maps of the blueshifted and redshifted SO (6₅–5₄) emission in I04169. The integrated velocity ranges for the blueshifted and redshifted emission are $V_{LSR} = 4.59 - 6.80$ km s⁻¹ and $6.80 - 9.01$ km s⁻¹, respectively. Contour levels are in steps of 3σ , where the 1σ noise level is 42 mJy beam⁻¹ km s⁻¹. A filled ellipse at the bottom-right corner shows the synthesized beam ($1''.82 \times 1''.52$; P.A. = -88°). c) Maps of the low-velocity blueshifted and redshifted C^{18}O (2–1) emission superposed on the 0.9-mm dust-continuum image in I04169. The integrated velocity ranges are $V_{LSR} = 5.68 - 6.80$ km s⁻¹ and $6.80 - 7.64$ km s⁻¹ for the blueshifted and redshifted emission, respectively. Contour levels are in steps of 2σ , where 1σ noise levels are 55 mJy beam⁻¹ km s⁻¹ and 48 mJy beam⁻¹ km s⁻¹ for the blueshifted and redshifted emission, respectively. A filled ellipse at the bottom-right corner shows the synthesized beam ($3''.09 \times 2''.90$; P.A. = -69°). d) Map of the high-velocity blueshifted ($V_{LSR} = 4.28 - 5.68$ km s⁻¹) C^{18}O (2–1) emission. Contour levels are in steps of 2σ ($1\sigma = 62$ mJy beam⁻¹ km s⁻¹).

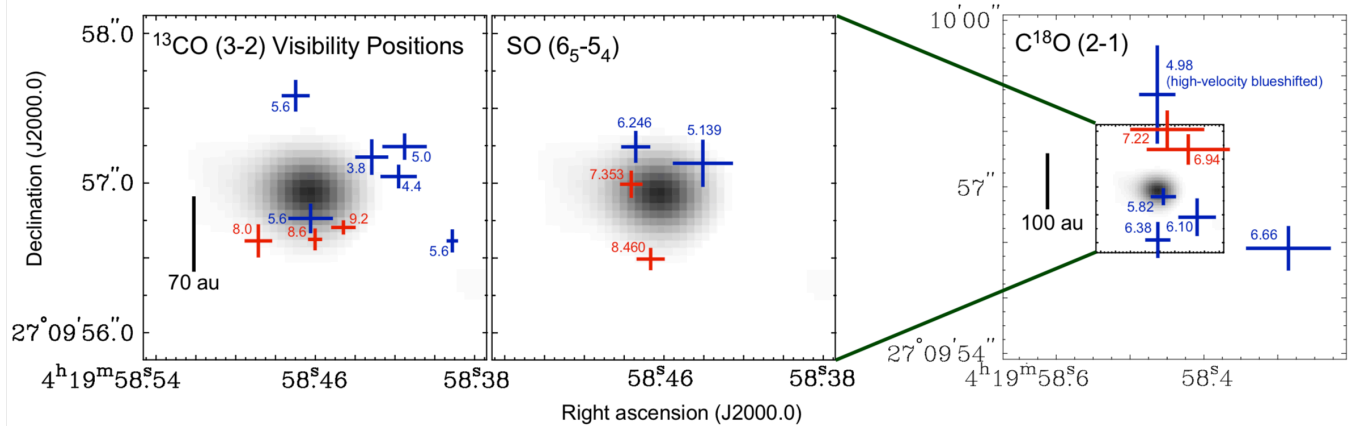


Figure 7. Plots of the peak position of the ^{13}CO (3–2) (left panel), SO ($6_5\text{--}5_4$) (middle), and C^{18}O (2–1) emission (right) at each velocity, as derived from direct fitting of 2-dimensional Gaussian functions to the visibilities. Blue and red crosses denote the peak positions of the blueshifted and redshifted emission, respectively, and the number next to each cross shows the LSR velocity. Lengths of the crosses denote the fitting errors. Background gray scales show the 0.9-mm continuum image (same as Figure 1a).

Table 5. Summary of the Velocity Gradients around I04169 along the Major Axis

Molecular Line	Radius (au)	Velocity Gradient (NW – SE)	References
C^{18}O (1–0)	~ 1000	Red – Blue	Ohashi et al. (1997)
C^{18}O (2–1)	~ 400	Red – Blue	This work
SO ($6_5\text{--}5_4$)	~ 200	Blue – Red	This work
^{13}CO (3–2)	~ 100	Blue – Red	This work

3.3. Position - Velocity Diagrams

Figures 8a and b show Position - Velocity (P-V) diagrams of the C^{18}O (2–1) (green contours) and SO ($6_5\text{--}5_4$) emission (red) passing through the protostellar position along the major axis (NW - SE), superposed on the ^{13}CO (3–2) P-V diagram (black). The cut line of the P-V diagrams is shown in Figure 6. The ^{13}CO P-V diagram along the major axis shows that the blue and redshifted emission are spatially separated with respect to the protostellar position. The spatial and velocity locations of the ^{13}CO emission overlap with the Keplerian rotation curve around the central stellar mass of $0.1 M_{\odot}$ (see dashed curves in Figure 8), although the limited sensitivity and spatial dynamical range of the present SMA data prevent us from deriving the radial profile of the gas motion. Within the velocity range where the ^{13}CO emission is significantly suppressed, the C^{18}O emission shows that the northwestern part is redshifted and southeastern part blueshifted. The sign of this C^{18}O velocity gradient is opposite to that of the ^{13}CO emission. In the higher blueshifted velocity there is an additional C^{18}O emission component, which appears to connect to the blueshifted ^{13}CO emission.

Figure 8b shows that the high-velocity ($\gtrsim V_{\text{sys}} \pm 0.8 \text{ km s}^{-1}$) SO emission appears to be closely correlated with the ^{13}CO emission, and the high-velocity blueshifted SO emission is located to the northwest and the redshifted emission southeast. On the other hand, in the lower-velocity range ($\lesssim V_{\text{sys}} \pm 0.8 \text{ km s}^{-1}$) the extended SO emission appears to trace a similar velocity feature to that traced by the C^{18}O emission.

Figures 9a and b compare the P-V diagrams of the ^{13}CO (3–2) (black contours), C^{18}O (2–1) (green), and the SO ($6_5\text{--}5_4$) (red) emission along the minor axis. As described above, the C^{18}O (2–1) emission shows a slight velocity gradient along the minor axis too, where the southwestern part is blueshifted and the northeastern part redshifted (Figure 9a). Since the associated molecular outflow is blue- and redshifted to the southwest and northeast (Figure 2), the southwestern and northeastern parts of the flattened protostellar envelope perpendicular to the outflow must be on the far- and near side. Thus, the C^{18}O emission exhibits the blueshifted emission on the far side and redshifted

emission on the near side, which can be interpreted as an infalling gas motion on the flattened envelope. Based on this concept, free-fall curves on the mid-plane with the central protostellar mass of 0.5, 0.1, and 0.01 M_{\odot} are drawn in the P-Vs. Whereas the limited spatial resolution and sensitivity of the $C^{18}O$ image cube prevent us from making conclusive discussion, the $C^{18}O$ velocity gradient along the minor axis seems to be better traced with the free-fall curve with the central mass lower than 0.1 M_{\odot} . The P-V diagram of the SO emission along the minor axis does not show a clear velocity gradient, in contrast with the P-V diagram along the major axis.

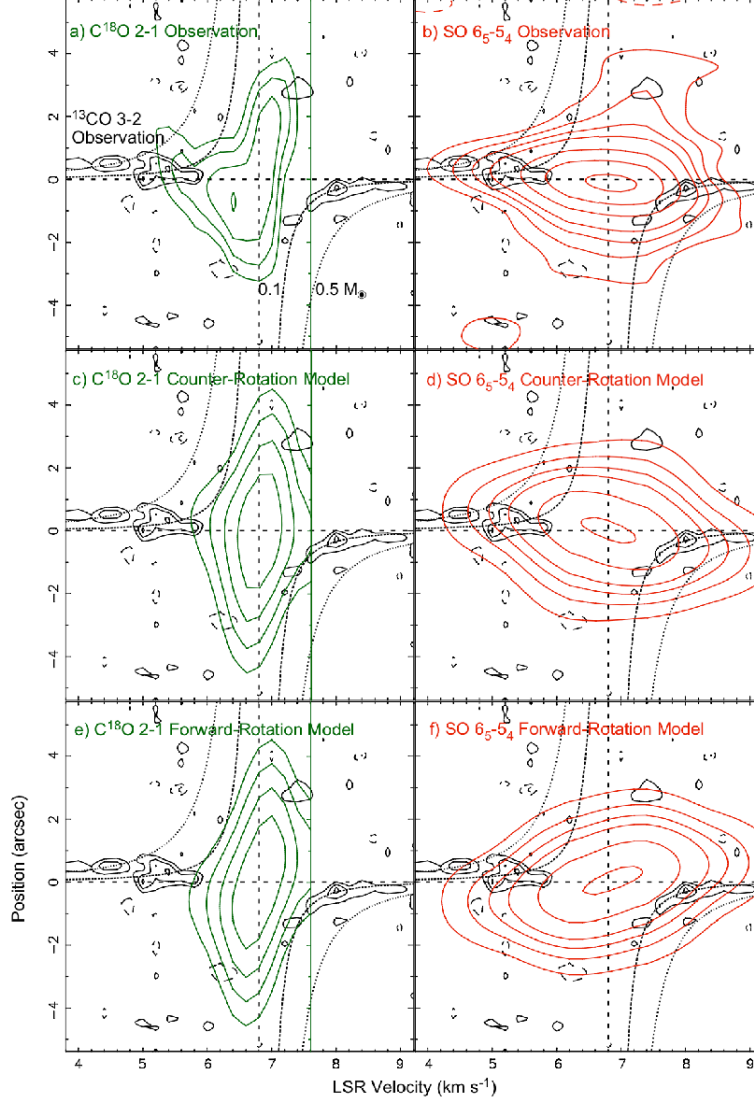


Figure 8. a) Observed Position - Velocity (P-V) diagrams of the ^{13}CO (3-2) (black contour) and $C^{18}O$ (2-1) emission (green) in I04169 along the major axis (P.A. = 154°) passing through the protostellar position. Contour levels of the ^{13}CO P-V start from 2σ in steps of 1σ ($1\sigma = 0.12 \text{ Jy beam}^{-1}$), and those of the $C^{18}O$ P-V from 3σ in steps of 1σ ($1\sigma = 0.099 \text{ Jy beam}^{-1}$). Vertical and horizontal dashed lines denote the systemic velocity of 6.8 km s^{-1} and the protostellar position, respectively. Dashed curves show Keplerian rotation curves with $i = 60^{\circ}$ and the central protostellar masses of $0.1 M_{\odot}$ and $0.5 M_{\odot}$ as labeled. The rightmost green vertical line delineates the spectral range covered with the present SMA $C^{18}O$ (2-1) data. b) Observed P-V diagram of the SO (6_5-5_4) emission in I04169 along the major axis passing through the protostellar position (red contours), overlaid on the P-V diagram of the ^{13}CO (3-2) emission (black contours). Contour levels of the SO emission are 2σ , 4σ , 6σ , 8σ , and then in steps of 4σ ($1\sigma = 0.027 \text{ Jy beam}^{-1}$). c) P-V diagram of the $C^{18}O$ (2-1) emission along the major axis obtained from the counter-rotating model. Contour levels are the same as those of the observed P-V diagram. d) P-V diagram of the SO (6_5-5_4) emission along the major axis obtained from the same counter-rotating model as that of the $C^{18}O$ (2-1) model. Contour levels are the same as those of the observed P-V diagram. e) and f) P-V diagrams of the $C^{18}O$ (2-1) and SO (6_5-5_4) emission, respectively, obtained from the forward-rotating model.

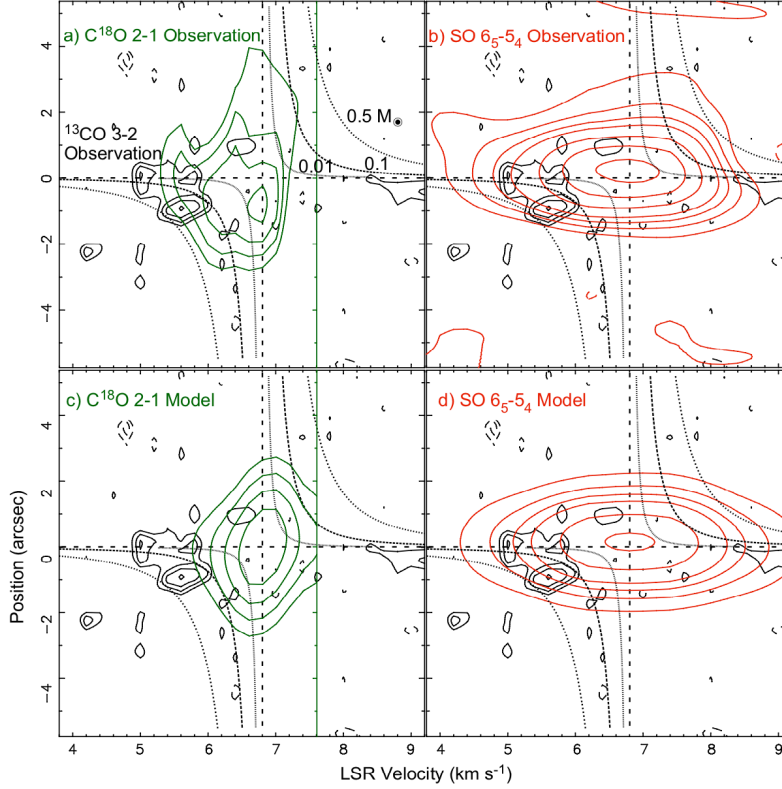


Figure 9. a) Observed P-V diagram of the C^{18}O (2–1) emission in I04169 along the minor axis (P.A. = 64°) passing through the protostellar position (green contours), overlaid on the P-V diagram of the ^{13}CO (3–2) emission (black). Contour levels of the C^{18}O emission start from 3σ in steps of 1σ ($1\sigma = 0.099 \text{ Jy beam}^{-1}$), and those of the ^{13}CO (3–2) emission from 2σ in steps of 1σ ($1\sigma = 0.12 \text{ Jy beam}^{-1}$). Vertical and horizontal dashed lines denote the systemic velocity of 6.8 km s^{-1} and the protostellar position, respectively. Dashed curves show free-fall curves with $i = 60^\circ$ and the central protostellar masses of $0.01 M_\odot$, $0.1 M_\odot$ and $0.5 M_\odot$ as labeled. The rightmost green vertical line delineates the spectral range covered with the present SMA C^{18}O (2–1) data. b) Observed P-V diagram of the SO (6₅–5₄) emission in I04169 along the minor axis (P.A. = 64°) passing through the protostellar position (red contours), overlaid on the P-V diagram of the ^{13}CO (3–2) emission (black). Contour levels of the SO emission are 2σ , 4σ , 6σ , 8σ , and then in steps of 4σ ($1\sigma = 0.027 \text{ Jy beam}^{-1}$). c) and d) Model P-V diagrams of the C^{18}O (2–1) and SO (6₅–5₄) emission, respectively. Contour levels are the same as those of the corresponding observed P-V diagrams.

3.4. Line Profiles

Figure 10 shows the SMA line profiles toward the protostellar position of I04169. The brightness temperature of the ^{12}CO (2–1) line is scaled by a factor of $1/3$ for more direct comparison between the ^{12}CO (2–1) and SO (6₅–5₄) line. The ^{12}CO (2–1) line profile exhibits a blueshifted high-velocity wing until $V_{LSR} \lesssim 0.0 \text{ km s}^{-1}$, consistent with our interpretation that the ^{12}CO (2–1) emission traces the molecular outflow. In the redshifted part there is only a marginal hint of the wing, but the U-shaped spatial distribution of the redshifted ^{12}CO (2–1) emission (see Figure 2a) suggests that the origin of the redshifted ^{12}CO (2–1) emission is also the molecular outflow. The SO (6₅–5₄) line does not show such a wing component, but a single peak at around the systemic velocity, where the ^{12}CO (2–1) emission is largely suppressed. While the signal-to-noise ratio is limited, no clear blueshifted wing is identified in the the ^{13}CO (3–2) spectrum. Around the systemic velocity the ^{13}CO (3–2) emission is significantly suppressed, presumably due to the presence of a foreground absorbing material. Such a foreground absorber can also explain the absorption features in the ^{12}CO (2–1) and ^{13}CO (2–1) spectra at the same velocities. The peak velocity of the blueshifted ^{13}CO (3–2) line ($V_{LSR} \sim 5.5 \text{ km s}^{-1}$) is located where the ^{12}CO (2–1) emission becomes deficient. Comparison between the ^{12}CO (2–1) and ^{13}CO (3–2) velocity channel maps at the same angular resolution shows that the peak positions and the systematic velocity structures are different between the ^{12}CO (2–1) and ^{13}CO (3–2) emission. These results imply that the nature of the ^{13}CO (3–2) and SO (6₅–5₄) emission is distinct from that of the ^{12}CO (2–1) emission (*i.e.*, outflow), and that the ^{13}CO (3–2) and SO (6₅–5₄) emission most likely trace a circumstellar gas component.

From the two isotropic lines of the ^{13}CO (2–1) and C^{18}O (2–1) emission, the excitation temperature and the optical

depths of the molecular lines can be estimated by solving the following simultaneous equations, on the assumption that both the ^{13}CO (2–1) and C^{18}O (2–1) emission trace the same gas component and are in the LTE condition,

$$T_B^{13} = (J_{\nu_{13}}(T_{\text{ex}}) - J_{\nu_{13}}(T_{bg}))(1 - \exp(-f_r \tau_{18})), \quad (2)$$

$$T_B^{18} = (J_{\nu_{18}}(T_{\text{ex}}) - J_{\nu_{18}}(T_{bg}))(1 - \exp(-\tau_{18})), \quad (3)$$

where T_B^X , ν_X , τ_X ($X=13$ or 18) are the brightness temperature, line frequency, and the optical depth of the ^{13}CO (2–1) or C^{18}O (2–1) emission. T_{ex} is the excitation temperature, which is common between the ^{13}CO (2–1) and C^{18}O (2–1) emission on the assumption of the LTE condition, and T_{bg} is the background temperature ($=2.725$ K). f_r is the ratio of the ^{13}CO and C^{18}O molecular abundance, and is adopted to be $f_r = 7.3$ (Wilson & Rood 1994). Around the systemic velocity, the ^{13}CO (2–1) brightness temperature becomes below the C^{18}O (2–1) brightness temperature, suggesting that the ^{13}CO (2–1) emission also suffers from the effect of the foreground absorbing material. In these velocity regions it is not possible to estimate T_{ex} and τ_{18} from the above equations. Thus, T_{ex} and τ_{18} are estimated at bluer velocities, and at $V_{LSR} = 5.8, 6.1,$ and 6.4 km s $^{-1}$ T_{ex} is estimated to be 7.8, 7.5, and 6.9 K, and τ_{18} 0.43, 0.61, and 0.87, respectively. We note, however, that there is likely a significant contamination from the outflow component to the ^{13}CO (2–1) emission (Figure 2), which makes this simple one-zone LTE analysis infeasible. On the other hand, the observed peak brightness temperature of the C^{18}O (2–1) emission ($\lesssim 1.6$ K) is well below the anticipated gas temperature of the protostellar envelope (~ 20 K) (Aso et al. 2015; Harsono et al. 2015), which suggests that the C^{18}O (2–1) emission is likely optically thin.

The SO (6 $_5$ –5 $_4$) image cube is convolved to have the same angular resolution as that of the ^{13}CO (2–1) and C^{18}O (2–1) image cubes shown in Figure 10, and T_{ex} of the SO (6 $_5$ –5 $_4$) line is assumed to be the same as derived above ($=7.8$ K). Then, the optical depth of the SO (6 $_5$ –5 $_4$) emission is estimated to be 0.26, 1.10, 1.15, and 0.13 at $V_{LSR} = 5.1, 6.2, 7.4,$ and 8.5 km s $^{-1}$, respectively. The estimated SO (6 $_5$ –5 $_4$) optical depth is likely an upper limit, as the SO (6 $_5$ –5 $_4$) emission traces the inner, denser molecular gas than that traced by the C^{18}O (2–1) emission and the excitation temperature of the SO (6 $_5$ –5 $_4$) emission is likely higher than that of the C^{18}O (2–1) emission. These results indicate that the SO (6 $_5$ –5 $_4$) emission is also optically thin or marginally optically thick. Therefore, the effects of the optical depths on the gas kinematics traced by these two lines are likely negligible.

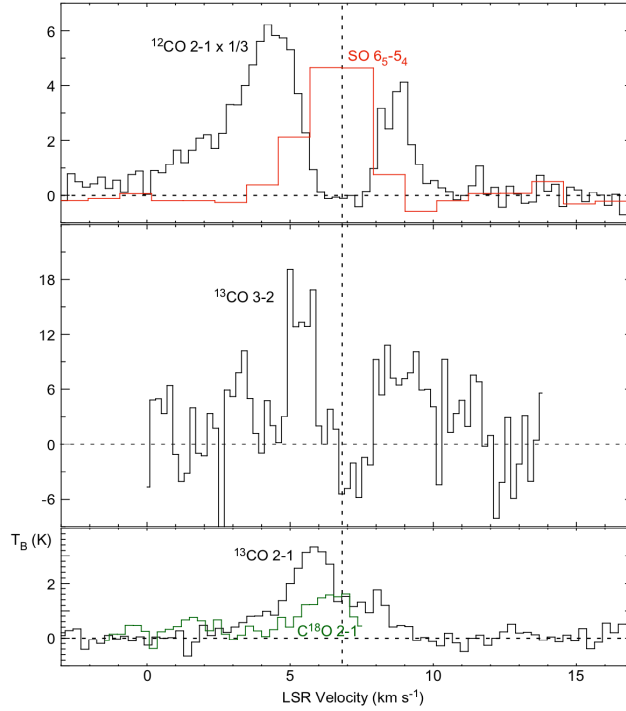


Figure 10. SMA spectra toward the protostellar position of I04169. For direct comparison, the beam sizes of the ^{12}CO (2–1) and ^{13}CO (2–1) spectra are smoothed to those of the SO (6 $_5$ –5 $_4$) and C^{18}O (2–1) spectra, respectively (see Table 3). Vertical and horizontal dashed lines denote the systemic velocity of 6.8 km s $^{-1}$ and the spectral baseline, respectively.

4. ANALYSIS

The SMA image cubes in a set of the molecular emission toward I04169 exhibit distinct velocity structures at different spatial scales. To investigate the nature of these velocity structures, we constructed geometrically-thin envelope-disk models in the C¹⁸O (2–1) and SO (6₅–5₄) emission. As the purpose of our model is to reproduce the observed gas motions in the inner $\lesssim 500$ au scale around the protostar, geometrically-thin assumption is likely valid. Even at a larger scale, the C¹⁸O (1–0) emission shows a 2200 au \times 1100 au scale elongated envelope around the protostar, and the major axis of the envelope is perpendicular to the associated outflow axis (Ohashi et al. 1997). The outflow is well developed with a wide opening angle ($>40^\circ$; Figure 2a) at around the apex. These observational results imply that dense gas distribution within $r \sim 1000$ au from the protostar is likely flattened. Furthermore, our modeling of protostellar envelopes and disks around the other protostellar sources as observed with ALMA reveals that geometrically-thin envelope / disk models reproduce the observed features reasonably well (*e.g.*, Aso et al. 2015; Yen et al. 2017; Takakuwa et al. 2017). The formation of so-called pseudo-disks is also expected from several MHD simulations (Machida et al. 2011a; Harsono et al. 2015; Tomida et al. 2015).

The protostellar envelope around I04169 as seen in the C¹⁸O (1–0) emission is approximated to be a 2-dimensional Gaussian with the FWHM sizes along the major \times minor axes of $16'' \times 8''$ and the position angle of 154° (Ohashi et al. 1997). Thus, the model moment 0 maps of the C¹⁸O (2–1) and SO (6₅–5₄) emission are assumed to be single 2-dimensional Gaussians with the same axis ratio (*i.e.*, inclination angle $i = \arccos \frac{8''}{16''} = 60^\circ$) and the position angle. The peak position of the model C¹⁸O (2–1) moment 0 map is fixed to be the protostellar position as measured from the 0.9-mm continuum emission with the Natural weighting (Figure 1), while that of the model SO (6₅–5₄) moment 0 map the peak position of the observed SO moment 0 map derived from the 2-dimensional Gaussian fitting. The intrinsic emission extents (*i.e.*, the size of the Gaussians) and the flux densities are unknown parameters, as the observed images are processed through the interferometric filtering. Thus, these two parameters for each of the C¹⁸O and SO emission are treated as free parameters. Hereafter we call these free parameters “emission parameters”.

In contrast with the emission parameters, parameters for gas motions should be common in the C¹⁸O and SO models. The model gas motions are divided into two regimes, the inner Keplerian-rotating disk and the outer, rotating and infalling envelope. Keplerian rotation motion with the central stellar mass of $0.1 M_\odot$ is incorporated within the Keplerian-disk radius, which is treated as a free parameter. The spatial-velocity locations of the ¹³CO (3–2) emission are consistent with those expected from the Keplerian rotation with the central stellar mass of $0.1 M_\odot$, while the limited signal-to-noise ratio and the spatial and spectral resolutions prevent us from investigating the radial profile of the gas motion (see Figure 8). Outside the Keplerian disk a rotating and infalling protostellar envelope is present. The rotating and infalling velocities of the envelope are simply assumed to be uniform, and are regarded as free parameters. In reality, the rotating and infalling velocities must have certain radial profiles (Krasnopolsky et al. 2011; Li et al. 2014; Tsukamoto et al. 2015b). The spatial and spectral dynamic ranges of the present SMA image cubes are, however, not high enough to discuss such radial profiles, and in our model constant infalling and rotating velocities are adopted as proxies of the averaged gas motions in the envelope. Both forward- and counter-rotations of the disk with respect to the envelope rotation are attempted in our model. The internal velocity dispersion ($\equiv \sigma_{gas}$) of the envelope is fixed to be 0.4 km s^{-1} (Takakuwa et al. 2013; Takakuwa et al. 2015), whereas that of the disk is treated as a free parameter. We call these free parameters to represent gas motions “dynamical parameters”.

In our modeling, the model moment 0 maps of the C¹⁸O and SO emission are first produced with a given set of the emission parameters. Then, with a given set of the dynamical parameters, the model velocity channel maps of the C¹⁸O and SO emission are produced. Since the model envelope and disk are assumed to be geometrically thin and co-planar, with the given dynamical parameters the central velocity and the line width at each position are determined. It is thus straightforward to create model velocity channel maps of the C¹⁸O and SO emission. The produced model velocity channel maps are converted into visibility data with the same uv coverage, field of view, and the spectral channels of the real SMA observations. The model visibility data are then Fourier-transformed and CLEANed with the same imaging parameters as those for the real observational data (see Table 3). In this interferometric modeling process, visibility noises are not included for simplicity and for direct comparison with the observed images. Finally the model interferometric velocity channel maps of the C¹⁸O and SO emission are compared to the real velocity channel maps, and the residual velocity channel maps are made. Two kinds of residual velocity channel maps are produced. One is the observed velocity channel maps minus the model velocity channel maps. This sort of the residual maps is straightforward for interpretation, but is affected by the interferometric imaging process. The other is made from the observed visibilities minus the model image components or observed minus model visibilities. The subtracted

visibilities are Fourier-transformed without any deconvolution process.

Since there are a number of free parameters and our modeling includes SMA interferometric sampling and imaging, it is not practical to perform full χ^2 fitting of the model velocity channel maps to the observed velocity channel maps. Instead, we manually changed and adjusted the emission and dynamical parameters and tried to find a decent parameter set which reasonably reproduces the observed velocity channel maps both in the C¹⁸O and SO emission. Strictly, a more complete search for the parameter space and proper assessment of the χ^2 value are required to prove which model (forward- or counter-rotating models) is quantitatively better. Thus, our modeling effort cannot definitely show which model is statistically better, but just show a possible, plausible representation of the observed data. Our searching results are summarized in Table 6.

Table 6. Model Parameters

Parameter	Value	Fixed/Searching ^a
Systemic Velocity	$V_{LSR} = 6.8 \text{ km s}^{-1}$	Fixed
Inclination i	60°	Fixed
Position Angle θ	154°	Fixed
Envelope σ_{gas}	0.4 km s^{-1}	Fixed
Central Stellar Mass of the Keplerian Rotation	$0.1 M_\odot$	Fixed
Keplerian Radius	200 au	Searching
Disk σ_{gas}	1.0 km s^{-1}	Searching
Envelope Infalling Velocity	0.16 km s^{-1}	Searching
Envelope Rotational Velocity	0.2 km s^{-1}	Searching
FWHM size of the C ¹⁸ O emission along the major axis	$5''2$	Searching
C ¹⁸ O Integrated Flux Density	3.9 Jy km s^{-1}	Searching
FWHM size of the SO emission along the major axis	$2''7$	Searching
SO Integrated Flux Density	2.8 Jy km s^{-1}	Searching

^a “Fixed” indicates the fixed model parameters. “Searching” indicates the manually searched parameters from the comparisons between the model velocity channel maps and the observed channel maps.

Figures 11 and 12 compare the observed, model, and the residual velocity channel maps of the C¹⁸O emission for the counter- and forward-rotating models, respectively. In both models the rotation and infall of the envelope are common, but the rotational direction of the central disk is opposite. In the model velocity channel maps of Figures 11 and 12, the disk components appear at $V_{LSR} = 5.54\text{--}5.82 \text{ km s}^{-1}$ to the north and south of the protostar, respectively. Since the observed C¹⁸O emission in these velocities are weak, the flip of the rotational direction of the model disk does not produce meaningful differences in the residual maps. In the lower blueshifted velocities ($6.10\text{--}6.66 \text{ km s}^{-1}$), the emission centroid of both models appears to be located to the south of the protostar, while in the redshifted velocities ($6.94\text{--}7.22 \text{ km s}^{-1}$) to the north. These features in the model C¹⁸O velocity channel maps are originated from the envelope, and the systematic emission shift along the velocity traces that in the real observed velocity channel maps. Since the bulk of the C¹⁸O (2–1) emission is originated from the envelope and the emission originated from the disk is minimal, there is no significant difference between the counter- and forward-rotating models in the residuals. The rms of the residual channel maps is $0.105 \text{ Jy beam}^{-1}$ and $0.125 \text{ Jy beam}^{-1}$ in the image-based and visibility-based residuals for both models (The observational noise level is $0.099 \text{ Jy beam}^{-1}$).

Figures 13 and 14 show the observed, model, and the residual velocity channel maps of the SO emission for the counter- and forward-rotating models, respectively. The observed SO velocity gradient is opposite to that of the low-velocity C¹⁸O emission. The model with the disk rotational direction opposite to that of the envelope (Figure 13) reproduces the observed emission peak shift from north (blueshifted) to south (redshifted). On the other hand, the forward-rotation model shows a completely opposite sign of the velocity gradient (Figure 14). The residual images show “mirror-symmetric” residual patterns, and in such a sense the counter-rotating model appears a better representation of the SO velocity channel maps. Note that the spatial resolution in the SO velocity channel maps is higher than that of the C¹⁸O velocity channel maps shown in Figures 11 and 12. The velocity resolution of the SO velocity channel maps is, on the other hand, much coarser than that of the C¹⁸O velocity channel maps. These observational differences reproduce the apparent differences of the image cubes in the C¹⁸O and SO emission. In the image domain the rms

of the residual SO channel maps is $0.033 \text{ Jy beam}^{-1}$ for the counter-rotating model and $0.054 \text{ Jy beam}^{-1}$ for the forward-rotating model (the observational noise level is $0.027 \text{ Jy beam}^{-1}$). In the visibility domain, the rms are $0.046 \text{ Jy beam}^{-1}$ and $0.048 \text{ Jy beam}^{-1}$ for the counter-rotating and forward-rotating models, respectively. The rms of the residual maps made from the visibility subtraction does not show a significant difference between the counter-rotating and forward-rotating models, as neither model is a perfect representation of the observations derived from the complete parameter search. In such a sense, our modeling effort cannot prove that the counter-rotating model is statistically better than the forward-rotating model.

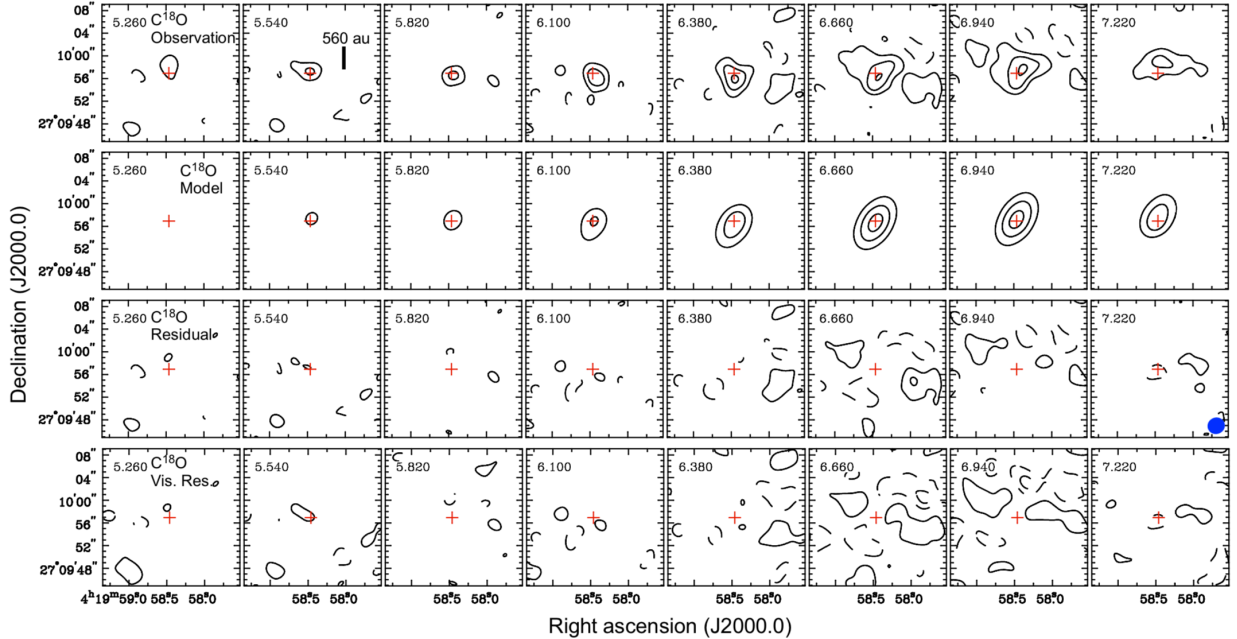


Figure 11. Comparison of the observed and model velocity channel maps of the C^{18}O (2–1) emission in I04169. Upper, upper-middle, lower-middle, and lower panels show the observed, model, residual velocity channel maps in the image domain, and the velocity channel maps of the residual visibilities, respectively. Contour levels are in steps of 2σ ($1\sigma = 0.099 \text{ Jy beam}^{-1}$).

To further investigate the model and observational results, the model P-V diagrams along the major and minor axes are shown in Figures 8 and 9, respectively. Comparisons between Figures 8a and c and between Figures 8b and d show that the shapes of the observed P-V diagrams resemble those of the counter-rotating model, which exhibit “tilted diamond” shapes. The forward-rotation model shown in Figures 8e and f does not reproduce such features in the P-V diagrams, and the P-Vs of the forward-rotation model are always skewed toward the two opposite quadrants. Along the minor axis, the observed C^{18}O P-V diagram exhibits a slight velocity gradient. This velocity gradient can be reproduced with a slow infalling velocity of 0.16 km s^{-1} in the model. This infalling velocity corresponds to the free-fall velocity with the central mass of $0.01 M_{\odot}$ at $r = 700 \text{ au}$ (see dashed curves in Figure 9). The observed and model P-V diagrams of the SO emission along the minor axis do not show any clear velocity gradient, consistent with our model interpretation that the SO emission primarily traces the central disk component.

Our model results are not from thorough numerical parameter fitting but obtained from manual parameter tuning. Thus our counter-rotating model is not guaranteed to be an unique, best-fit solution. There are no significant differences of the residual rms between the forward- and counter-rotating models, and in such a sense our modeling effort failed to show that the counter-rotating model is statistically better than the forward-rotating model. Nevertheless, the counter-rotating model reproduces the observed velocity gradient in the SO emission and the difference from that of the C^{18}O emission, which is not reproduced with the forward-rotating model. As the presence of the opposite velocity gradients is likely significant, our counter-rotating model can still provide one possible, plausible interpretation of the observed velocity structures. Figure 15 shows a schematic picture of the counter-rotating model.

5. DISCUSSION

5.1. Nature of the Detected Velocity Features

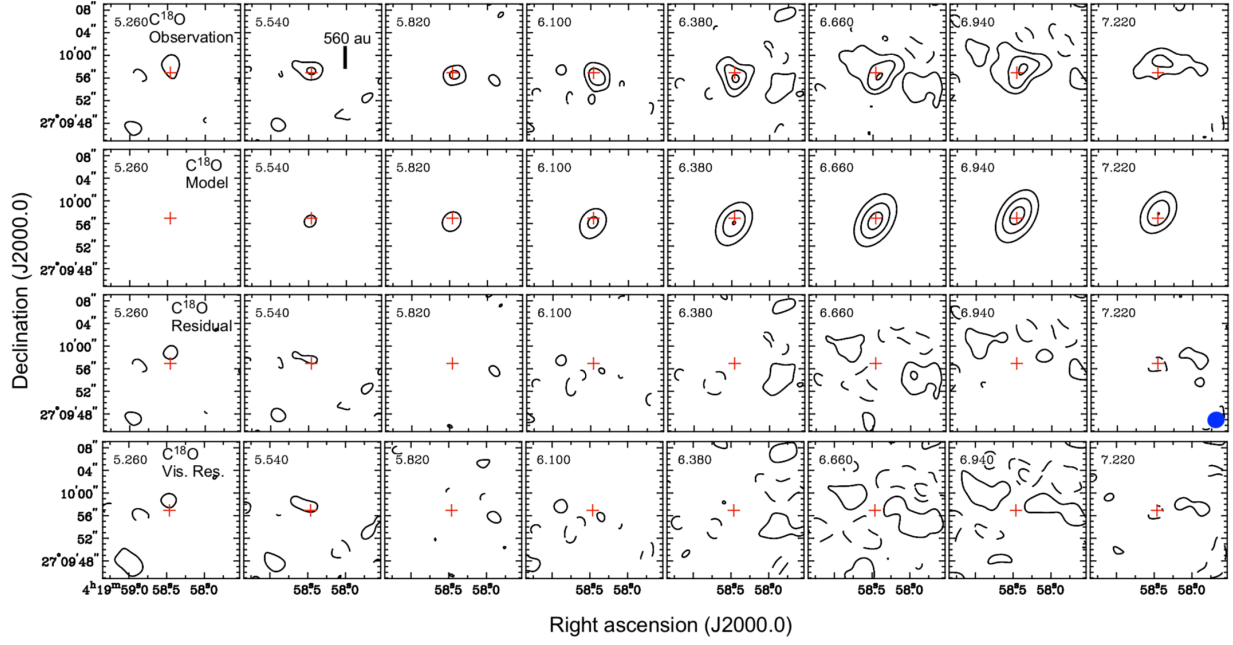


Figure 12. Same as that of Figure 11, but for the model of the forward rotation of the Keplerian disk.

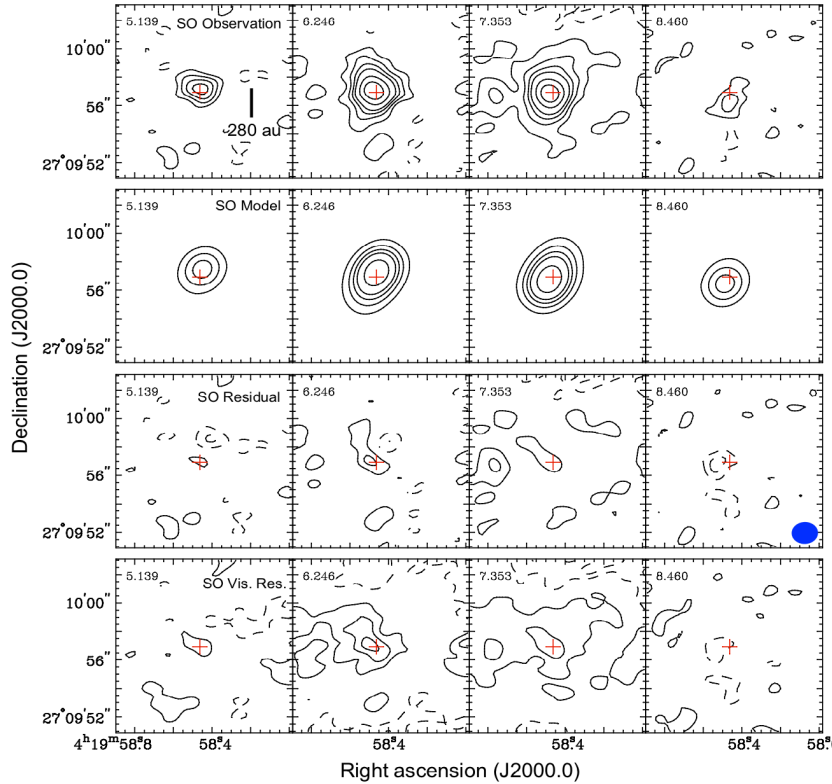


Figure 13. Comparison of the observed and model velocity channel maps of the SO (6_5-5_4) emission in I04169. Upper, upper-middle, lower-middle, and lower panels show the observed, model, residual velocity channel maps in the image domain, and the velocity channel maps of the residual visibilities, respectively. Contour levels are the same as those of Figure 4.

The molecular-line data toward I04169 reveal distinct velocity features at different spatial scales. At $r \sim 400 - 1000$ au, the northwestern part is redshifted and the southeastern part blueshifted, as traced by the C^{18}O ($2-1$; $1-0$) lines (see Table 5). In the inner $r \lesssim 200$ au the northwestern part becomes blueshifted and the southeastern part redshifted,

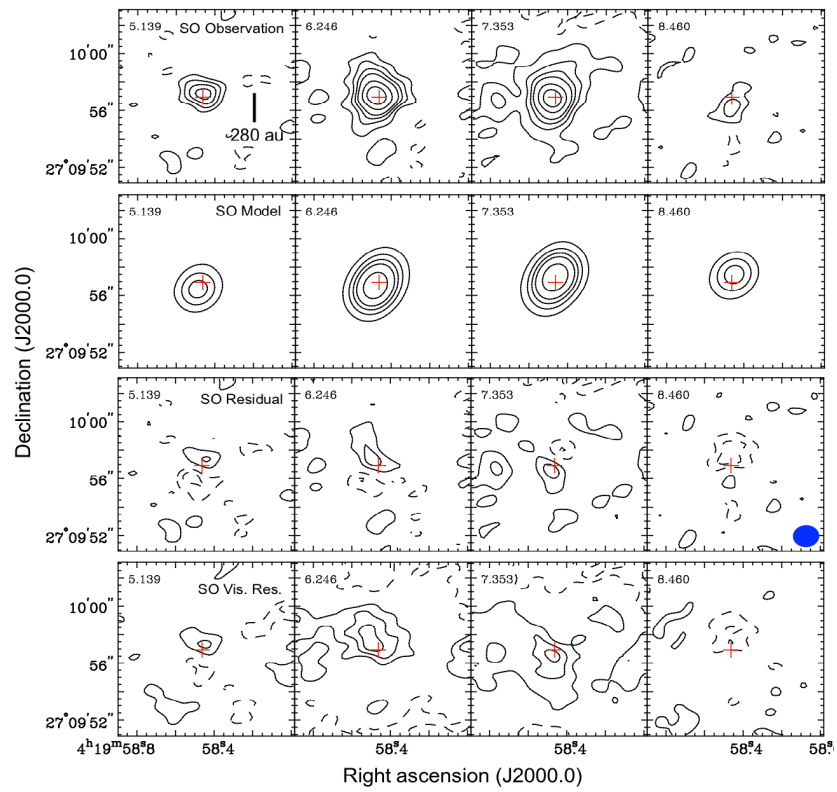


Figure 14. Same as that of Figure 13, but for the model of the forward rotation of the Keplerian disk.

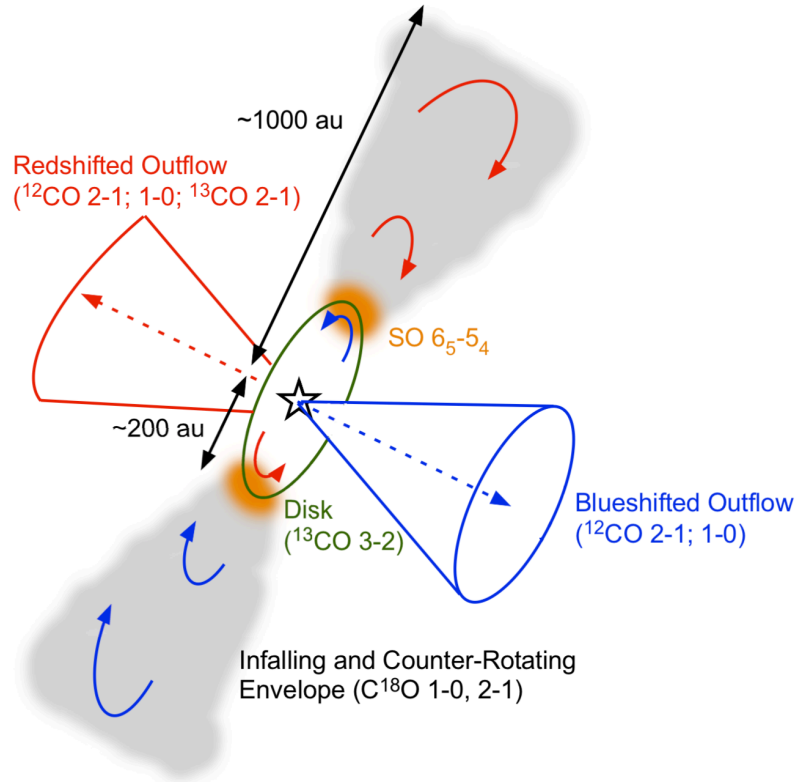


Figure 15. Schematic picture of I04169 inferred from the present SMA observations.

as seen in the SO (6_5-5_4) and ^{13}CO ($3-2$) emission. Our toy model shows that the observed velocity features can be reproduced with a system of the central disk plus the outer counter-rotating, infalling envelope, although our simple modeling effort cannot prove that the counter-rotating model is significantly better than the forward-rotating model in a quantitative way.

A possible source to change directions of velocity gradients is turbulence. Recent theoretical simulations of magnetized and turbulent collapsing dense cores show that turbulences produce additional angular momenta and induce magnetic diffusions and reconnections (Santos-Lima et al. 2012; Joos et al. 2013; Seifried et al. 2013; Matsumoto et al. 2017). These effects reduce relative strengths of magnetic braking and thus promote disk formation around the central stars. The axis of the formed disk (or the angular-momentum vector) can be misaligned from the that of the magnetic field, outflow, and the envelope (Matsumoto et al. 2017). Observationally, Harsono et al. (2014) conducted PdBI observations of disks around low-mass protostars, and compared the rotational directions of the $r \sim 100$ au scale disks to the directions of the velocity gradients of the dense cores as seen in the N_2H^+ emission observed with FCRAO (Caselli et al. 2002). The comparison between the $r \sim 100$ au scale disks and ~ 10000 au scale cores shows that there are indeed differences of the directions of the velocity gradients between the disks and cores, and the differences range from $\sim 90^\circ$ to $\sim 230^\circ$. Such differences of the velocity gradients between the large-scale cores and disks can be attributed to the effect of the turbulences. It is also possible that the identified change of the direction of the velocity gradients in I04169 is due to the turbulence. Presence of multiple gas clumps, which have different motions and velocities, can also reproduce the observed, apparent flip of the velocity gradients in I04169.

If the interpretation of the counter rotation is correct, the effect of magnetic fields is a promising source to realize such a velocity structure. The physical mechanism to produce such a counter rotation through magnetic fields is known as the Hall effect, one of the non-ideal MHD effects (Wardle 2004; Wardle & Salmeron 2012; Braiding & Wardle 2012a; Braiding & Wardle 2012b). In collapsing cloud cores, the Hall effect induces toroidal (or azimuthal component of) magnetic fields from poloidal magnetic fields at the mid-plane of the pseudo-disk or the flattened envelope. The induced toroidal field exerts the magnetic torque and the gas rotation with the left-handed screw direction of the global poloidal field in the case of the negative Hall resistivity. If the Hall induced magnetic torque is large enough and has an opposite direction to the initial rotation (this corresponds to the case in which the poloidal magnetic field direction is parallel to the angular momentum of the cloud core), the gas rotation can flip. The counter rotating structure also appears even when the direction of the Hall induced magnetic torque is the same as that of the initial rotation. In this case, the midplane of the envelope and the disk maintains the initial rotation direction, but the upper envelope exhibits the counter rotation due to the back reaction of the Hall induced forward rotation at the midplane. In both cases, the flattened envelope or pseudo-disk with the scale of ~ 100 AU can exhibit the counter rotation (Krasnopolsky et al. 2011; Li et al. 2011; Tsukamoto et al. 2015b; Wurster et al. 2016; Tsukamoto et al. 2017). Whether the Hall effect can induce the counter rotation or not depends on the magnetic field strength of the parent cloud core. Previous theoretical studies have shown that the counter rotation is realized in the cores with the mass-to-flux ratio $\lambda \sim 5$ (Li et al. 2011; Tsukamoto et al. 2015b; Tsukamoto et al. 2017). Here λ is normalized by its critical value. The Hall effect is more effective under a stronger magnetic field (*i.e.*, lower λ), and the previous observations of the magnetic fields in dense cores have found $\lambda \sim 2$ (Troland & Crutcher 2008; Crutcher 2012). Thus, the flip of the rotational direction caused by the Hall effect is likely possible under a typical condition of cloud cores. The magnetic field strength can be estimated from given λ as $B = 7.6 \times 10^{-21} N(\text{H}_2) \lambda^{-1} \mu\text{G}$ (Troland & Crutcher 2008). Toward I04169 $N(\text{H}_2)$ value is estimated to be $1.4 \times 10^{22} \text{ cm}^{-2}$ (Motte & André 2001), and $\lambda \sim 2$ yields the field strength of $54 \mu\text{G}$.

The limited spatial resolution and dynamic range of the present SMA data, however, prevent us from discriminating these different interpretations. If further higher-dynamic range observations of I04169 unveil the consistency of the velocity gradient from $r \sim 1000$ au down to 400 au scale and then the flip of the velocity gradient below 400 au, such results must be a strong evidence for the presence of counter rotation between the disk and envelope and the magnetic-field origin. In these spatial scales, theoretical simulations show that the possible range of the misalignment between the central disk and the outer envelope originated from turbulence is at most $\sim 30^\circ$ (Matsumoto et al. 2017). Unless the core mass is as high as $100 M_\odot$, the misalignment does not show a complete flip *i.e.*, 180° (Seifried et al. 2013). Thus, if the future higher-dynamic range observations unveil a systematic, consistent velocity structure and a flip of the velocity gradient simultaneously, that can rule out the origin of turbulence or multiple gas components. In addition, a more thorough theoretical modeling (not toy model) and statistical parameter search are required to prove that the counter rotation caused by the magnetic effect is the most probable and unique interpretation.

5.2. Implications of the Opposite Velocity Gradients

The present SMA observations of the Class I protostar I04169 have found that at different spatial scales the directions of the velocity gradients are opposite. With our simple model, we suggest that one of the intriguing interpretations is counter rotation between the protostellar envelope and disk caused by the magnetic fields, whereas we admit that at this stage we cannot exclude the other possible explanations.

Furthermore, a marginal, slow infalling velocity ($\sim 0.16 \text{ km s}^{-1}$) in the envelope has been identified. The identified infalling velocity corresponds to the free-fall velocity toward the central mass of $\sim 0.01 M_{\odot}$ or smaller at $r \lesssim 700$ au. If the mass of the central protostar is $0.1 M_{\odot}$ as inferred from the ^{13}CO (3–2) and SO (6₅–5₄) results and our modeling, the observed infalling velocity is much smaller than the corresponding free-fall velocity. Such small infalling velocities around the central disks have also been seen in the other protostellar objects from our recent ALMA observations (Ohashi et al. 2014; Aso et al. 2015). These results have been interpreted as the transitions from the infalling envelopes to the central disks with the increasing centrifugal support. The physical origin of the slow infalling velocity may also be the effect of magnetic fields (Li et al. 2011; Machida et al. 2011b).

Opposite velocity gradients at different spatial scales have also been seen in the other protostellar sources. In HL Tau, the $r \sim 100$ au scale protoplanetary disk exhibits blueshifted emission to the southeast of the protostar and redshifted emission to northwest (ALMA Partnership et al. 2015). On the contrary, the follow-up ALMA observations by Yen et al. (2017b) have found that the southeastern part of the $r \sim 1000$ au envelope around the protoplanetary disk of HL Tau as seen in the ^{13}CO (2–1) emission is redshifted and the northwestern part blueshifted. While Yen et al. (2017b) argued that a simple counter-rotating model is not sufficient to fully reproduce the observed gas motions, presence of opposite signs of the velocity gradients is identified with the ALMA observations. Among the protostellar sample investigated by Harsono et al. (2014), L1527 IRS shows almost a complete flip ($\sim 177^{\circ}$) of the velocity gradient between the core and the disk. Tobin et al. (2011) have also found that the northern part of the $r \sim 8000$ -au scale protostellar envelope around L1527 IRS is blueshifted and the southern part redshifted, and that in the inner $r \sim 1000$ -au scale the direction of the velocity gradient flips. The larger-scale velocity gradient is consistent with the result from the single-dish C_3H_2 (2₁₂–1₀₁; 2₀₂–1₁₁) observations (Takakuwa et al. 2001), and interferometric observations of L1527 IRS have confirmed the presence of the $r \lesssim 100$ au scale Keplerian disk with the opposite velocity gradient (Tobin et al. 2012; Sakai et al. 2014; Ohashi et al. 2014; Aso et al. 2017). In these two cases the differences of the spatial scales are within an order of magnitude. These results imply that our SMA results of I04169 are not unique.

While both turbulences and magnetic fields have been considered to play a vital role in star and circumstellar-disk formation out of cloud cores, it has been difficult to observationally identify such effects in protostellar sources. Radial rotational profiles in the protostellar envelopes have been measured observationally to study gas motions into circumstellar-disk formation (*e.g.*, Harsono et al. 2014; Yen et al. 2017a). Whereas these observations show that the radial rotational profiles in the envelopes and disks can be approximated to be $v_{rot} \sim r^{-1}$ (*i.e.*, rotation with the conserved specific angular momenta) and $\sim r^{-0.5}$ (Keplerian rotation), the rotational profiles measured from these observations are not accurate enough to be directly compared with those from theoretical simulations including magnetic fields and turbulence. Thus, it is not straightforward to infer the impact of magnetic fields and turbulence from the observed rotational profiles, if the direction of the rotational vector is common in the envelopes and disks. By contrast, the flip of the velocity gradient, if present, is rather easy to identify observationally. We thus suggest that further (re-)investigation of the opposite velocity gradients of molecular gas around protostellar sources should shed new light on the studies of star and circumstellar-disk formation.

6. SUMMARY

We have made high-resolution ($\sim 0''.5$) SMA observations of the Class I protostar I04169 in the ^{13}CO (3–2) line and the 0.9-mm dust continuum emission. We have also reduced and imaged the SMA archival data of I04169 in the ^{12}CO (2–1), ^{13}CO (2–1), C^{18}O (2–1) and the SO ($J_N = 6_5$ –5₄) lines and the 1.3-mm continuum emission at angular resolutions of $2''$ – $3''$. Compilation of these SMA data provides us with the following new insights of the circumstellar materials around I04169.

1. Both the 0.9-mm and 1.3-mm continuum emission are barely resolved, and the extent of the 0.9-mm continuum emission is $\lesssim 0''.3 \sim 40$ au. The spectral index β is estimated to be low (~ 0 – 0.5), suggesting presence of dust growths. The mass of the dusty component is estimated to be $0.0042 - 0.024 M_{\odot}$ for $T_d = 10 - 30$ K. The redshifted ^{12}CO (2–1) emission exhibits a tilted *U*-shaped feature with its symmetric axis pointing toward the northeast of the protostar, and the blueshifted ^{12}CO (2–1) emission *V*-shaped feature toward the southwest. The ^{12}CO (2–1) spectrum toward the protostellar position exhibits a blueshifted high-velocity wing until $V_{LSR} \lesssim 0.0 \text{ km s}^{-1}$. These results suggest that the ^{12}CO (2–1) emission traces the molecular outflow driven from I04169.

The position angle of the outflow axis is almost orthogonal to that of the $r \sim 1000$ -au protostellar envelope associated with I04169 as seen in the C^{18}O (1–0) emission (P.A.= 154°). The redshifted ^{13}CO (2–1) emission appears to trace the same redshifted outflow component as that traced by the ^{12}CO (2–1) emission, while the blueshifted ^{13}CO (2–1) emission a distinct, compact feature to the northwest of the protostar.

2. The high-resolution ^{13}CO (3–2) image cube shows that the blue- ($V_{LSR} = 3.7 - 5.9 \text{ km s}^{-1}$) and redshifted ($7.5 - 9.3 \text{ km s}^{-1}$) emission are located to the northwest and southeast of the protostar, respectively, with the outermost emission extent of $r \sim 100$ au. The direction of the ^{13}CO (3–2) velocity gradient is almost orthogonal to that of the associated molecular outflow, and thus along the major axis. The peak locations of the blueshifted and redshifted SO (6₅–5₄) emission are consistent with those of the ^{13}CO (3–2) emission. On the other hand, the lower-resolution C^{18}O (2–1) image cube exhibits distinct velocity features in the low-velocity range ($5.7 - 7.6 \text{ km s}^{-1}$): The blue- and redshifted C^{18}O (2–1) emission are located to the south and north of the protostar, respectively, with the outermost extent of $r \sim 400$ au. Along the major axis (NW-SE), the sign of the velocity gradient of the C^{18}O (2–1) emission is opposite to that of the ^{13}CO (3–2) and SO (6₅–5₄) emission, but is consistent with that of the $r \sim 1000$ -au scale protostellar envelope. Such different velocity structures in the different molecular lines are also confirmed from the direct fitting to the visibility data in the individual velocity channels. Along the minor axis the C^{18}O (2–1) emission shows a marginal NE (red) - SW (blue) velocity gradient too. In the highly blueshifted velocity ($5.3 - 5.5 \text{ km s}^{-1}$), the C^{18}O (2–1) counterpart of the blueshifted ^{13}CO (3–2) emission is also present.
3. To interpret the observed velocity structures, we have constructed toy models of an infinitesimally-thin Keplerian disk plus envelope in the C^{18}O (2–1) and SO (6₅–5₄) emission, including the SMA imaging simulations. We tested models where the envelope and the inner disk are co-rotating and counter-rotating with each other. Our manual parameter search has found that the counter-rotating model better reproduces the observed velocity gradient in the SO emission. On the other hand, since our manual parameter search failed to obtain statistically significant fitting results with neither the counter-rotating and forward-rotating models, we could not verify that the counter-rotating model is significantly better than the forward rotating model. As the presence of the opposite velocity gradients between the C^{18}O and SO emission is likely significant, our counter-rotating model can still provide one possible, plausible interpretation of the observed velocity structures. Higher sensitivity, and higher spatial dynamic-range observations of I04169 along with a more detailed model, and a more complete exploration of the parameter space associated with these models, are needed to definitively demonstrate that a counter-rotating envelope/disk is a more proper model than a standard co-rotating envelope/disk model.
4. The observed velocity structures in the circumstellar material of I04169 can be interpreted as either turbulent gas motions, multiple gas clumps at different velocities, or counter rotation between the disk and envelope. With the present data we cannot define which is the most appropriate model. Nevertheless, we suggest that counter rotation between the disk and envelope caused by the effect of the magnetic fields is one of the intriguing interpretations for the observed flip of the direction of the velocity gradient. There are indeed other protostellar sources which exhibit the different velocity gradients between the disks and envelopes. While the effects of the magnetic fields have been considered to be critical in star and circumstellar-disk formation, it has been difficult to observationally identify such effects in protostellar sources. The counter rotation could be a promising observational signature to investigate the magnetic effects. Higher-sensitivity and higher spatial dynamic-range observations of protostellar envelopes and disks, along with (re-)investigation of the existing ALMA data of protostellar sources, should provide us with important insights of the effects of the magnetic fields, which have been difficult to identify observationally.

We would like to thank N. Ohashi and J. Lim for their fruitful discussions, and all the SMA staff supporting this work. S.T. acknowledges a grant from the Ministry of Science and Technology (MOST) of Taiwan (MOST 102-2119-M-001-012-MY3), and JSPS KAKENHI Grant Numbers JP16H07086 and JP18K03703 in support of this work.

Facilities: SMA

REFERENCES

- Allen, A., Li, Z.-Y., & Shu, F. H. 2003, *ApJ*, 599, 363
- ALMA Partnership, Brogan, C. L., Pérez, L. M., et al. 2015, *ApJL*, 808, L3
- Aso, Y., Ohashi, N., Saigo, K., et al. 2015, *ApJ*, 812, 27
- Aso, Y., Ohashi, N., Aikawa, Y., et al. 2017, *ApJ*, 849, 56
- Braiding, C. R., & Wardle, M. 2012a, *MNRAS*, 422, 261
- Braiding, C. R., & Wardle, M. 2012b, *MNRAS*, 427, 3188
- Caselli, P., Walmsley, C. M., Terzieva, R., & Herbst, E. 1998, *ApJ*, 499, 234
- Caselli, P., Benson, P. J., Myers, P. C., & Tafalla, M. 2002, *ApJ*, 572, 238
- Crutcher, R. M. 2012, *ARA&A*, 50, 29
- Eisner, J. A. 2012, *ApJ*, 755, 23
- Gillis, J., Mestel, L., & Paris, R. B. 1974, *Ap&SS*, 27, 167
- Hacar, A., Tafalla, M., Kauffmann, J., & Kovács, A. 2013, *A&A*, 554, A55
- Harsono, D., Jørgensen, J. K., van Dishoeck, E. F., et al. 2014, *A&A*, 562, A77
- Harsono, D., van Dishoeck, E. F., Bruderer, S., Li, Z.-Y., & Jørgensen, J. K. 2015, *A&A*, 577, A22
- Hennebelle, P., & Ciardi, A. 2009, *A&A*, 506, L29
- Hildebrand, R. H. 1983, *QJRAS*, 24, 267
- Ho, P. T. P., Moran, J. M., & Lo, K. Y. 2004, *ApJL*, 616, L1
- Joos, M., Hennebelle, P., Ciardi, A., & Fromang, S. 2013, *A&A*, 554, A17
- Kenyon, S. J., Calvet, N., & Hartmann, L. 1993a, *ApJ*, 414, 676
- Kenyon, S. J., Whitney, B. A., Gomez, M., & Hartmann, L. 1993b, *ApJ*, 414, 773
- Krasnopolsky, R., Li, Z.-Y., & Shang, H. 2011, *ApJ*, 733, 54
- Li, Z.-Y., Krasnopolsky, R., & Shang, H. 2011, *ApJ*, 738, 180
- Li, Z.-Y., Krasnopolsky, R., Shang, H., Zhao, B. 2014, *ApJ*, 793, 130
- Lindberg, J. E., Jørgensen, J. K., Brinch, C., et al. 2014, *A&A*, 566, A74
- Machida, M. N., & Matsumoto, T. 2011a, *MNRAS*, 413, 2767
- Machida, M. N., Inutsuka, S.-I., & Matsumoto, T. 2011b, *PASJ*, 63, 555
- Machida, M. N., Matsumoto, T., & Inutsuka, S.-I. 2016, *MNRAS*, 463, 4246
- Masson, J., Chabrier, G., Hennebelle, P., Vaytet, N., & Commerçon, B. 2016, *A&A*, 587, A32
- Matsumoto, T., Machida, M. N., & Inutsuka, S.-I. 2017, *ApJ*, 839, 69
- Mellon, R. R., & Li, Z.-Y. 2008, *ApJ*, 681, 1356
- Motte, F., & André, P. 2001, *A&A*, 365, 440
- Mouschovias, T. C. 1985, *A&A*, 142, 41
- Nakano, T., Nishi, R., & Umebayashi, T. 2002, *ApJ*, 573, 199
- Nishi, R., Nakano, T., & Umebayashi, T. 1991, *ApJ*, 368, 181
- Ohashi, N., Hayashi, M., Ho, P. T. P., Momose, M., Tamura, M., Hirano, N., & Sargent, A. I. 1997, *ApJ*, 488, 317
- Ohashi, N., Saigo, K., Aso, Y., et al. 2014, *ApJ*, 796, 131
- Ossenkopf, V., & Henning, T. 1994, *A&A*, 291, 943
- Saito, M., Kawabe, R., Kitamura, Y., & Sunada, K. 2001, *ApJ*, 547, 840
- Sakai, N., Sakai, T., Hirota, T., et al. 2014, *Nature*, 507, 78
- Santos-Lima, R., De Gouveia Dal Pino, E. M., & Lazarian, A. 2012, *ApJ*, 747, 21
- Sault, R. J., Teuben, P. J., & Wright, M. C. H. 1995, *Astronomical Data Analysis Software and Systems IV*, ASP Conference Series, Vol. 77, R. A. Shaw, H. E. Payne, & J. J. E. Hayes, eds., p.433
- Scoville, N. Z., Carlstrom, J. E., Chandler, C. J., et al. 1993, *PASP*, 105, 1482
- Seifried, D., Banerjee, R., Pudritz, R. E., & Klessen, R. S. 2013, *MNRAS*, 432, 3320
- Simon, M., Dutrey, A., & Guilloteau, S. 2000, *ApJ*, 545, 1034
- Tafalla, M., & Hacar, A. 2015, *A&A*, 574, A104
- Takakuwa, S., Kawaguchi, K., Mikami, H., & Saito, M. 2001, *PASJ*, 53, 251
- Takakuwa, S., Saito, M., Lim, J., & Saigo, K. 2013, *ApJ*, 776, 51
- Takakuwa, S., Kiyokane, K., Saigo, K., & Saito, M. 2015, *ApJ*, 814, 160
- Takakuwa, S., Saigo, K., Matsumoto, T., et al. 2017, *ApJ*, 837, 86
- Tatematsu, K., Umemoto, T., Kandori, R., & Sekimoto, Y. 2004, *ApJ*, 606, 333
- Tobin, J. J., Hartmann, L., Chiang, H.-F., et al. 2011, *ApJ*, 740, 45
- Tobin, J. J., Hartmann, L., Chiang, H.-F., Wilner, D. J., Looney, L. W., Loinard, L., Calvet, N., and D'Alessio, P. 2012, *Nature*, 492, 83
- Tomida, K., Okuzumi, S., & Machida, M. N. 2015, *ApJ*, 801, 117
- Troland, T. H., & Crutcher, R. M. 2008, *ApJ*, 680, 457
- Tsukamoto, Y., Iwasaki, K., Okuzumi, S., Machida, M. N., & Inutsuka, S. 2015a, *MNRAS*, 452, 278
- Tsukamoto, Y., Iwasaki, K., Okuzumi, S., Machida, M. N., & Inutsuka, S. 2015b, *ApJL*, 810, L26
- Tsukamoto, Y., Okuzumi, S., Iwasaki, K., Machida, M. N., & Inutsuka, S. 2017, *PASJ*, 69, 95
- Umebayashi, T., & Nakano, T. 1990, *MNRAS*, 243, 103
- Wardle, M. 2004, *Ap&SS*, 292, 317
- Wardle, M., & Salmeron, R. 2012, *MNRAS*, 422, 2737
- Williams, J. P., & Cieza, L. A. 2011, *ARA&A*, 49, 67
- Wilner, D. J., & Welch, W. J. 1994, *ApJ*, 427, 898
- Wilson, T. L., & Rood, R. 1994, *ARA&A*, 32, 191
- Wurster, J., Price, D. J., & Bate, M. R. 2016, *MNRAS*, 457, 1037
- Yen, H.-W., Takakuwa, S., Ohashi, N., & Ho, P. T. P. 2013, *ApJ*, 772, 22
- Yen, H.-W., Koch, P. M., Takakuwa, S., et al. 2017a, *ApJ*, 834, 178
- Yen, H.-W., Takakuwa, S., Chu, Y.-H., et al. 2017b, *A&A*, 608, A134
- Young, C. H., Shirley, Y. L., Evans II, N. J., & Rawlings, J. M. C. 2003, *ApJS*, 145, 111